Universidad Politécnica de Madrid

Master's Thesis

Object tracking using direct methods in RGB-D cameras

Author:
Isaac Sánchez

Supervisor:
Luis Baumela

A thesis submitted in fulfilment of the requirements
for the degree of Master Universitario en Inteligencia Artificial

in the

July 2015

"Every day I remind myself that my inner and outer life are based on the labors of other men, living and dead, and that I must exert myself in order to give in the same measure as I have received and am still receiving."

Albert Einstein

UPM

Resumen

Escuela Técnica Superior de Ingenieros Informáticos
Departamento de Inteligencia Artificial

Master Universitario en Inteligencia Artificial

Seguimiento de objetos mediante métodos directos con cámaras RGB-D

por Isaac Sánchez

En esta tesis se presenta un análisis en profundidad de cómo se deben utilizar dos tipos de métodos directos, Lucas-Kanade e Inverse Compositional, en imágenes RGB-D y se analiza la capacidad y precisión de los mismos en una serie de experimentos sintéticos. Éstos simulan imágenes RGB, imágenes de profundidad (D) e imágenes RGB-D para comprobar cómo se comportan en cada una de las combinaciones. Además, se analizan estos métodos sin ninguna técnica adicional que modifique el algoritmo original ni que lo apoye en su tarea de optimización tal y como sucede en la mayoría de los artículos encontrados en la literatura. Esto se hace con el fin de poder entender cuándo y por qué los métodos convergen o divergen para que así en el futuro cualquier interesado pueda aplicar los conocimientos adquiridos en esta tesis de forma práctica. Esta tesis debería ayudar al futuro interesado a decidir qué algoritmo conviene más en una determinada situación y debería también ayudarle a entender qué problemas le pueden dar estos algoritmos para poder poner el remedio más apropiado. Las técnicas adicionales que sirven de remedio para estos problemas quedan fuera de los contenidos que abarca esta tesis, sin embargo, sí se hace una revisión sobre ellas.

UPM

Abstract

Escuela Técnica Superior de Ingenieros Informáticos
Departamento de Inteligencia Artificial

Master Universitario en Inteligencia Artificial

Object tracking using direct methods in RGB-D cameras

by Isaac Sánchez

This thesis presents an in-depth analysis about how direct methods such as Lucas-Kanade and Inverse Compositional can be applied in RGB-D images. The capability and accuracy of these methods is also analyzed employing a series of synthetic experiments. These simulate the effects produced by RGB images, depth images and RGB-D images so that different combinations can be evaluated. Moreover, these methods are analyzed without using any additional technique that modifies the original algorithm or that aids the algorithm in its search for a global optima unlike most of the articles found in the literature. Our goal is to understand when and why do these methods converge or diverge so that in the future, the knowledge extracted from the results presented here can effectively help a potential implementer. After reading this thesis, the implementer should be able to decide which algorithm fits best for a particular task and should also know which are the problems that have to be addressed in each algorithm so that an appropriate correction is implemented using additional techniques. These additional techniques are outside the scope of this thesis, however, they are reviewed from the literature.

Agradecimientos

Me gustaría agradecer a Luis todos los ratos que me ha ayudado a entender la materia, a sus discusiones y en especial, a su paciencia y sus constantes ganas y ánimos que me han llevado a terminar satisfactoriamente este trabajo.

Agradezco también a todos los profesores que me han ayudado a progresar en cada uno de los distintos enfoques que ellos han adoptado sobre la vida, sobre esta ciencia, la informática, e incluso de cualquier otra rama de la ciencia en general. Gracias a ellos, creo tener una mejor capacidad de contrastar ideas, evaluar situaciones y sobre todo afrontar los problemas con una mayor creatividad. Sin ellos no podría llegar a pensar con la misma claridad con la que a día de hoy puedo. Y esto es un privilegio del que no todo el mundo puede disfrutar.

Doy gracias también a toda la comunidad de software libre ya que sin ellos, la cantidad de informáticos bien formados se habría visto impactada considerablemente al no poder disfrutar de la libertad de enteder el software producido por otros. Aparte de esto, les doy las gracias puesto que sin sus esfuerzos, la totalidad de las tareas realizadas en esta tesis no se habría podido llevar a cabo.

Doy las gracias a mis padres y a toda mi familia en general puesto que sin su ayuda ni su apoyo no podría haber conseguido ninguno de los objetivos que me he marcado a lo largo de mi vida. Además, no me cabe ninguna duda de que sin la libertad y el constante apoyo de los que he disfrutado, es muy probable que no hubiese ni siquiera llegado a elegir y seguir este camino.

Y por supuesto, también doy las gracias a todos mis allegados incluyendo a todos mis amigos, que me han apoyado incondicionalmente y me han acompañado en mis risas y soportado mis penas.

Contents

List of Figures

Abbreviations

RGB-D	**R**ed **G**reen **B**lue - **D**epth
AAM	**A**ctive **A**ppearance **M**odel
SLAM	**S**imultaneous **L**ocalization **A**nd **M**apping
ICP	**I**terative **C**losest **P**oint
LK	**L**ucas - **K**anade algorithm
IC	**I**nverse **C**ompositional algorithm
BCS	**B**rightness **C**onstancy **A**ssumption
EBCS	**E**xtended **B**rightness **C**onstancy **A**ssumption
ToF	**T**ime **o**f **F**light

Symbols

P	point in world coordinates
P_T	point in world coordinates after transformation
P_C	point in camera coordinates
P_S	point in screen coordinates
T_{6dof3D}	3D rigid body transformation matrix of 6 dof
K	camera intrinsics matrix
C	camera extrinsics matrix
I	input image(s) function(s) or matrix(ces)
T	template image function or matrix
x	a single point in space
$\mathcal{V}$	set of sample points in space
X	$\mathcal{V}$ in matrix form
$\mathcal{D}$	generic function domain
r	residual function or matrix
μ	single parameter or vector of parameters
$\mathcal{P}$	set of available parameters
$\delta\mu$	single parameter increment or vector of increments

$\mathcal{L}$	linearization function
J	Jacobian of the residual function, either function or matrix
$\mathcal{T}$	compositionally accumulated transformations in matrix form

A mis padres, José y Hortensia

Chapter 1

Introduction

Object tracking is an interesting field of research with multiple applications that range from surveillance in public places and military purposes to player pose tracking in media and entertainment or any sort of human-computer interaction. Object tracking is also interesting when applied together with object detection to be able not only to follow objects in images but also to identify these objects in arbitrary scenes. A special case of object tracking is *motion tracking* of faces and body gestures either with or without marks.

Localization is also a very important application that can take advantage of object tracking methods in general. Localization usually requires the identification of the scenario itself rather than a particular object in a scenario. This is useful for robot's self-localization so that they can estimate the position or at least the area where they are located. Localization has another application related to augmented reality. Localization is required so that the virtual models that are rendered over a background actually fit with the background's coordinate system.

This thesis analyzes the capability of direct methods performance in RGB-D images. These techniques can be used for common computer vision tasks such as object tracking, localization (see figure 1.1) or video mosaicing (see figure 1.2).

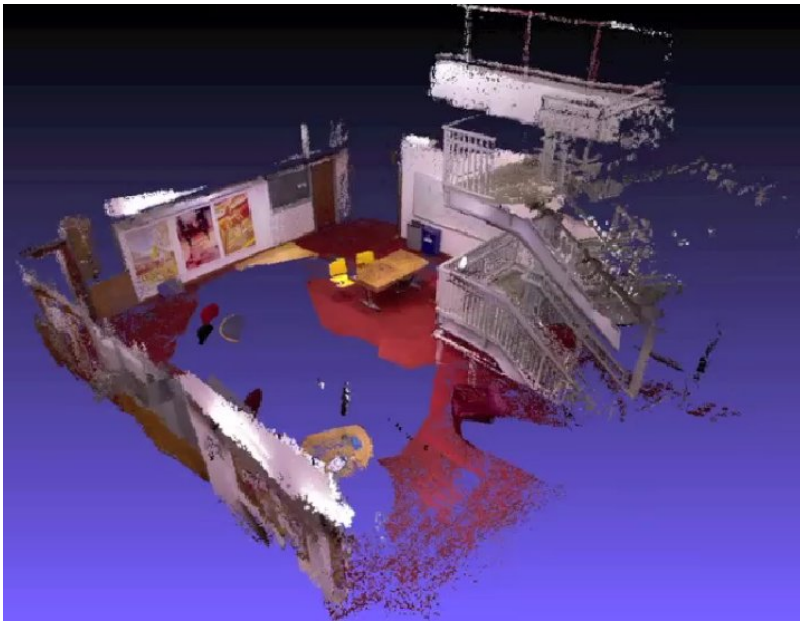

FIGURE 1.1: Localization and mapping image example obtained from https://groups.csail.mit.edu.

There are several other methods that can also accomplish these tasks and some of these methods will be reviewed in chapter 2. However, they are outside of the scope of this thesis. This thesis only concentrates on direct methods due to our belief that they can take advantage of the properties of depth based images.

1.1 Motivation

The Lucas-Kanade algorithm is one of the first and most well known direct image alignment algorithms in the literature. It is based on a Newton optimization that

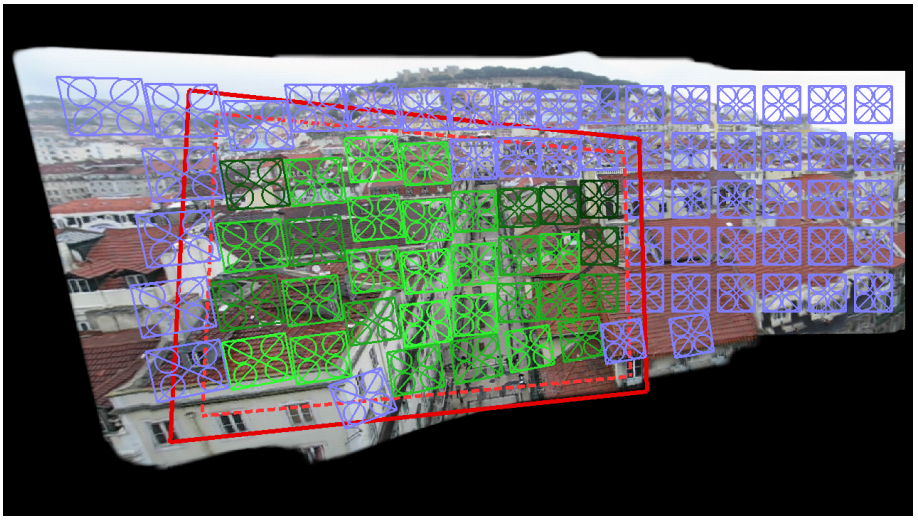

FIGURE 1.2: Video mosaicing image obtained from Google Images.

minimizes the discrepancies in the grey values of the aligned images. One drawback of this algorithm is its computational cost since it requires the calculation of a gradient for each pixel involved in the minimization.

The objective of this thesis is to evaluate the performance of direct methods for aligning RGBD images. We consider Lucas-Kanade as the baseline image alignment approach and compare it with the efficient Inverse Compositional algorithm. In our analysis we will consider depth images, gray-scale images and depth + gray-scale images.

The hypothesis of this thesis is that the Lucas-Kanade algorithm will be able to align all three types of images. The Inverse Compositional algorithm will be able to at least align depth images reasonably well but it should produce acceptable results in grey scale images that include depth data.

Chapter 2

Literature review

In this chapter we are going to review some of the main techniques related to image registration and object tracking. We are also going to briefly compare and highlight the most recent ones.

2.1 General misconceptions

Direct methods may not always be found in the literature under this name, they can also be found in other topics such as *image alignment* and *image registration methods*. The conceptual difference between direct methods and these other topics is that direct methods can be considered as generic and do not need to be applied explicitly to images. However, there is a clear distinction between image registration and *tracking* methods. When image registration methods are used, the goal is to align entire images via transformations. It is assumed that two images can be aligned if there exists a transformation that can convert one image into the other image. On the other hand, tracking methods are designed to find specified targets in the scene or to obtain their current position relative to the scene. But this does not mean that

they are mutually exclusive concepts, image registration and object tracking can be used for the same purpose. In this case, we say that we are using a *tracking-by-registration* approach [1]. However, tracking can be achieved using other methods like machine learning [1].

2.2 Image registration techniques

In image registration problems, images must be transformed so that all the points in the desired image match the values of all the corresponding points of another image. This is also known as *image alignment*. These values are usually the color values in greyscale.

Image registration techniques have been applied to a wide spectrum of applications like panoramic image mosaics [2, 3], pose estimation in aerial vehicles [4] or AAM fitting [5]. There are two extensive surveys related to image registration which are [6, 7]. There is also another good survey of image registration in the medical image context [8].

The approaches to solve image registration problems can be divided into two main families. These are the *direct methods* and the *feature-based methods*.

2.2.1 Direct methods

Direct methods are image registration techniques that try to minimize the *error* between the two input images in every single point. There are several ways to achieve this and also several error metrics that can be used. The main well-known approaches in direct methods are the Lucas-Kanade algorithm [9], Hager-Belhumeur algorithm [10], forward-compositional algorithm [11, 12] and the inverse-compositional algorithm [13, 14]. Most of these approaches require the calculation of the Jacobian

matrix analytically at least once at every frame. There are other techniques that find numericaly a linear regressor that aligns the images [15]. The difference between an analytic Jacobian and a numeric Jacobian will be addressed in chapter 4.

In general, direct methods can be classified into additve or compositional approaches and forward or inverse approaches. These are explained further in chapter 3. More techniques and applications can be found in the literature review in [1].

2.2.2 Feature-based methods

These methods follow the same goal as direct methods in image registration. The main difference is that instead of using the entire image, these methods use just a subset of points of interest or salient *features* that are considered useful for searching a corresponding feature in the other image. These must have some noticeable differences in comparison to other features of the same image since ambiguity is an undesirable effect and real world images tend to have large amounts of ambiguous points. Typically, these features do not depend on the camera's position or any other conditions such as illumination [1]. Some interesting references can be found as well in the literature review of [1].

2.3 Other object tracking and detection techniques

In this section, we review some existing techniques in the object tracking domain that are not considered as image registration. A very good reference of object tracking is the survey [16]. This article provides a vast review of methods including those related to object detection and tracking, segmentation, object representation and different feature selections. The image registration techniques are referenced inside template and density-based appearance models and optical flow sections. Another

useful reference is [17] because they provide a very extensive benchmark for object tracking.

2.4 Techniques in RGB-D images

Recently, devices known as RGB-D cameras have become increasingly popular and accesible to the public. This has encouraged researchers to use these sorts of devices for experimentation. We have found that these devices have been used essentially for object tracking and SLAM.

Among all the articles that are going to be reviewed in this section, the one that comprises a wider variety of techniques is a recent survey of RGB-D based visual odometry [18]. These techniques are compared and studied under different conditions and requirements. It combines techniques that use only color data, only depth data, both, bidimensional images, three-dimensional images, point clouds and also visual features. Those techniques that manage pointclouds for tracking or SLAM are usually classified as *dense mapping*.

Since 2010 a cheap RGB-D device has been brought to consumer level and it has also gained interest in the scientific community for the same reasons. This is the first Microsoft Kinect sensor which appeared as an additional item required to play certain videogames in the Microsoft Xbox 360. This has also encouraged other developers to create similar devices such as the Asus Xtion. The Kinect camera enables developers to use its motion sensing capabilities coupled with its middleware to track people's actions in front of the camera to a certain degree of freedom and detail. However, its use in our image registration context and SLAM became more prominent especially with the appearance of Kinect Fusion [19]. Kinect Fusion is the name given to the software developed at Microsoft that is capable or reconstructing an interior scenario using the Kinect depth sensor data with the aid of a computer

and a graphics accelerator. This is performed using the 3D texture capabilities of the graphics card to store the scenario as a 3D volume grid and the ICP algorithm assuming that most of the scene is not altered severely between consecutive frames. This permitted them to separate statical objects from dynamic objects since they assumed that the amount of the former were more in the scene than the amount of the latter. Therefore, dynamic objects were those points detected as outliers after the ICP algorithm converged. This feature was used in their second article [20] where they exploited these capabilities even further letting the user perform several interactions with their environment while being tracked.

In [21, 22] they make use of the Kinect sensor as well for their experiments. In [21] they propose a framework which is capable of calibrating the camera and tracking objects alike using the depth images retrieved by the Kinect sensor. Unlike the ICP algorithm, they use a level-set embedding function instead of a per-point energy function for the minimization. This set of points must fit the shape of adaptive primitive object models that serve as the unknown target model. In [22], this framework is extended further by substituting the energy function with a probabilistic version. Instead of adapting the primitives to an observed shape just via scaling, the adaptation is much more flexible, for example, allowing a box to become a shoe in terms of shape. Therefore, the initial shape of the model is only maintained temporarily and just required for the initialization. Apart from this, this framework benefits from a great parallelization potential (essential for efficient GPU acceleration) since there is no 2D projection required as in other techniques, thus, there is no depth testing, which goes against parallelization.

All these articles provide generic frameworks and techniques to use with low-cost RGB-D cameras especially in small indoor environments. As said before, RGB-D cameras have been used in SLAM as well to aid robots in self-localisation and mapping tasks. These tasks usually require to be optimised for larger spaces in comparison to those in previous articles presented in this document. Articles such

as [23, 24] present dense mapping algorithms tested in large environments with RGB-D spherical camera models and using grey and depth images for the optimisation instead of just using the latter. In [25], they implement a direct version of ICP which shares lots of similarities to any other common direct method, however, they give different weights to depth data and grey-scale data and they also apply weighting functions. This work is also continued in [26] where they treat all data equally and they also add several features to their tests. Another group of researchers have been using direct methods to perform SLAM experiments [27]. The main contribution of this article is their robustness estimation method. Instead of using common, state-of-the-art functions for robustness estimation, they observed that a *t-distribution* matched sensor noise data better than other distributions. In [28], their second article, they developed an algorithm that could decrease the amount of frames being processed without an extraordinary loss of accuracy as well as a path correction algorithm.

Several of the articles presented in the previous paragraph use a database that has been especially designed for SLAM testing purposes. This database is available publicly as well as some tools to evaluate the accuracy results against their ground-truth data [29].

Apart from the image registration techniques and pointcloud based techniques, there are other methods that have proved to be useful as well. For instance, in [30] they have used RGB-D cameras to create a large multi-view dataset of ordinary objects that have been used to train their machine learning algorithm for object detection. Machine learning and training techniques have been also succesfully used in conjunction with ICP to track objects with RGB-D cameras in [31]. In articles such as [32, 33], they use an approach that shares some similarities with common pointclouds. They use small patches which provide more information of the surface and they also provide occlusion in the area that the patch covers.

Chapter 3

Background

Theoretical background of direct methods and RGB-D cameras is provided in this chapter. It will be necessary so that the reader can understand the underlying concepts behind the experiments and implementations that we have performed and presented in this document.

3.1 Models

Models are used in *model-based tracking* as a series of assumptions made on the object or the scene or the relationship between both. According to [1], there are three different models:

- **Target model**: the assumption is made on the target's representation structure and data.
- **Motion model**: assumption on the target's motion also known as *kinematics*.

- **Camera model**: assumption on the virtual camera, we assume how the camera processes the data to create each frame (consecutive images).

These assumptions restrict the possible outcomes of the object, the scene and the retrieved images from the virtual camera in our implementations. These assumptions are made in order to efficiently process the object and the scene and also serve as a prior simplification of the problem, hence, if we are going to track deformable faces, we may consider using AAMs as the target model. Target models can be mainly divided into rigid models and deformable models.

The motion model (which we will also refer as *transformation*) serves the same objective, we want to simplify our search space so that tracking is not so relatively difficult for our algorithm. The motion model is related to the target model in the sense that not all transformations are possible for all models, for instance, we cannot transform a bi-dimensional object in a bi-dimensional space with a three dimensional motion model. Thus, both are related and we must know which sort of motion model or transformation fits which sort of model and viceversa.

3.1.1 2D affine transformations

Affine transformations are those kinds of transformations that have a linear component and a translation component. Both components transform vectors from $\mathbb{R}^2$ to $\mathbb{R}^2$. This means that a two dimensional vector $\vec{a} = (x_a, y_a)$ can be transformed into another two dimensional vector $\vec{b} = (x_b, y_b)$. However, linear transformations impose a restriction over the vector $\vec{0} = (0, 0)$ since this vector cannot be transformed into any other vector by a linear transformation, whereas an affine transformation can, it has the said translation component. Typical linear transformations are scales, rotations and skews.

An affine transformation of a point P can be represented as the function $\mathcal{A} : \mathbb{R}^2 \to \mathbb{R}^2$ and represented in matrix form as

$$\mathcal{A} : P = \begin{bmatrix} u \\ v \end{bmatrix} \to P' = \begin{bmatrix} u' \\ v' \end{bmatrix} = A \cdot \begin{bmatrix} u \\ v \end{bmatrix} + b \tag{3.1}$$

where

$$A = \begin{bmatrix} a_{11} & a_{12} \\ a_{21} & a_{22} \end{bmatrix} \quad b = \begin{bmatrix} b1 \\ b2 \end{bmatrix}$$

or alternatively extending the problem to a homogeneous space $\mathcal{A}_{\mathbb{P}} : \mathbb{P}^2 \to \mathbb{P}^2$

$$\mathcal{A}_{\mathbb{P}} : P = \begin{bmatrix} u \\ v \\ 1 \end{bmatrix} \to P' = \begin{bmatrix} u' \\ v' \\ 1 \end{bmatrix} = \begin{bmatrix} a_{11} & a_{12} & b1 \\ a_{21} & a_{22} & b2 \\ 0 & 0 & 1 \end{bmatrix} \cdot \begin{bmatrix} u \\ v \\ 1 \end{bmatrix} \tag{3.2}$$

The latter representation is a more concise form and it is the most common one since it only requires a single matrix product.

These transformations can be applied directly to images. Images are essentially planes that have values associated to coordinates. Additionally, the values outside the limits of the image (those coordinates that lie outside the limits we impose) are set to a default value. We define the function $\mathcal{I} : \mathbb{R}^2 \to \mathbb{R}$ as an evaluation function of a grey-scale image as follows.

$$\mathcal{I}(u, v) = \begin{cases} value(u, v) & \text{if } (u, v) \text{ inside of image} \\ default & \text{if } (u, v) \text{ outside of image} \end{cases} \tag{3.3}$$

If we use this definition, applying a transformation to an image means that we are transforming a function into another function. However, we can see it from a different perspective, a transformation to an image can be seen as the transformation

of the sample points that are going to be substituted in the formula from above. There is no need to express a function-to-function transformation. For instance, in this alternative, if we wanted to move the image to the left, we would need to move the sample points' coordinates to the right as illustrated similarly in figure 3.1.

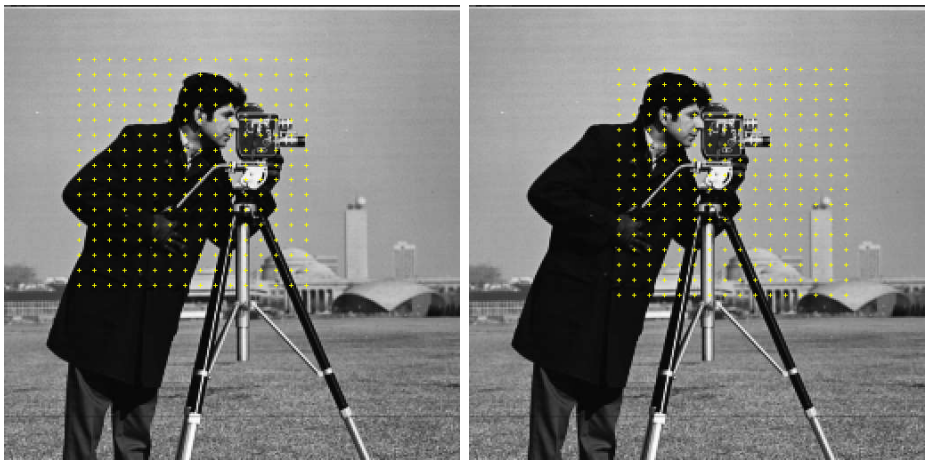

(A) Sample grid before transformation (B) Sample grid after moving image to the left

FIGURE 3.1: Classic cameraman image with sample points showing duality.

In the definition 3.3, we have not described how does the function *value* behave. In practice, images do not have infinite resolution and it is common to take samples from the image that do not match an exact coordinate with an existing value in the image. Thus, if we have a discrete image, we will have a discrete function $\mathcal{I}$. Since we may want to be able to sample non-discrete points that do not exactly match, we need to convert $\mathcal{I}$ into a non-discrete function. We may want, for example, to retrieve a value that is close to the values of the surrounding points. We can actually choose between a continuous function or a function with discontinuities such as in *nearest-neighbor* filtered images. Throughout the years, several techniques have been developed, such as *linear interpolation* between values of neighboring points. There are lots of ways to deal with this problem and choosing one method or another depends on the interest of the user.

3.1.2 3D transformations and pinhole camera model

In the cases presented in this document, we are going to concentrate mostly on 3D scenes and objects since that is what RGB-D cameras information give us about the environment. Therefore, we use the following assumptions:

- The target is a 3D rigid object represented as a set of sampled points that relate a position in space with data retrieved by the camera. These are also known as *point clouds*. Since the object is not deformable, a subset of points cannot move relatively to another subset of points, all points must move together as a whole set using the same transformation.
- The motion model has to be compatible with these 3D point clouds, thus, our motion model is a *3D rigid body transformation*.
- For the virtual camera, we are going to use the *pinhole-camera model* [34].

The motion model describes in this case how every single point of the point cloud is going to behave between two different frames or iterations separately. The 3D rigid body transformation can be applied separately to every single point as long as each point has at least the coordinates in the form (X, Y, Z) for a three dimensional space. Apart from the location data, point clouds can have additional data. In our case, that data can be intensity image values or color values. If we assume that we can separate the position data from the additional data in each point, we can perform the transformations using matrix algebra using homogeneous coordinates. The function $\mathcal{T}_{\text{6dof3D}} : \mathbb{P}^3 \to \mathbb{P}^3$ is defined as

$$\mathcal{T}_{\text{6dof3D}} : P \to P_T = T_{\text{6dof3D}} \cdot P \tag{3.4}$$

where

$$P_T = \begin{bmatrix} X_T \\ Y_T \\ Z_T \\ 1 \end{bmatrix} \quad T_{\text{6dof3D}} = \left[\begin{array}{c|c} R & \vec{t} \\ \hline \bar{0} & 1 \end{array}\right] \quad P = \begin{bmatrix} X \\ Y \\ Z \\ 1 \end{bmatrix}$$

The matrix T_{6dof3D} is the 3D rigid body transformation matrix of six degrees of freedom which are the three Euler angles expressed as the rotation matrix R and the three translation degrees of freedom in the three dimensional space. As the reader may note, points P and P_T have the said three coordinates and also have the forth coordinate set to 1. This forth coordinate is necessary to perform our transformation correctly in an affine manner and is also present in the transformation matrix. The expression of a location in four coordinates in this way as homogeneous coordinates. It is assumed that the reader is familiar with this concept and it is not explained any further.

The function that describes this rotation is $\mathcal{R} : \mathbb{R}^3 \to \mathbb{R}^3$. The associated matrix is the parametric rotation matrix R and is obtained using a product of rotation matrices in each axis as follows.

$$R \equiv R(\alpha, \beta, \gamma) = R_Z(\gamma) \cdot R_Y(\beta) \cdot R_X(\alpha) \tag{3.5}$$

where

$$R_X(\alpha) = \begin{bmatrix} 1 & 0 & 0 \\ 0 & \cos\alpha & -\sin\alpha \\ 0 & \sin\alpha & \cos\alpha \end{bmatrix} \quad R_Y(\beta) = \begin{bmatrix} \cos\beta & 0 & \sin\beta \\ 0 & 1 & 0 \\ -\sin\beta & 0 & \cos\beta \end{bmatrix}$$

$$R_Z(\gamma) = \begin{bmatrix} \cos\gamma & -\sin\gamma & 0 \\ \sin\gamma & \cos\gamma & 0 \\ 0 & 0 & 1 \end{bmatrix}$$

The parametric translation vector can be expressed as the transposed vector $\vec{t} \equiv \vec{t}(t1, t1, t3) = [t1\ t2\ t3]^T$.

Henceforth, the transformation can be seen as a matrix that is generated using those six parameters and the formula of T_{6dof3D} at the definition 3.4. The result is a parametric matrix of the form $T_{\text{6dof3D}}(\alpha, \beta, \gamma, t1, t1, t3)$.

Finally, we only need to specify the camera model. We are going to use the classic *pinhole-camera model* which can be expressed as the product of two parametric matrices, the camera intrinsics matrix K and the camera extrinsics matrix C. These two matrices are used in conjunction with the transformation matrix to generate the final transformation. The transformation of K and C together is known as *perspective projection* and can be noted as $\mathbf{p} : \mathbb{P}^3 \to \mathbb{P}^2$.

$$\mathbf{p} : P_C \to P_S = \left[\ K \ \middle|\ \bar{0}\ \right] \cdot \overbrace{C \cdot P_T}^{P_C} \tag{3.6}$$

where

$$P_S = \begin{bmatrix} \lambda j \\ \lambda i \\ \lambda \end{bmatrix} \quad K(f, k_u, k_v, s, i_0, j_0) = \begin{bmatrix} fk_u & s & j_0 \\ 0 & fk_v & i_0 \\ 0 & 0 & 1 \end{bmatrix}$$

$$P_C = \begin{bmatrix} X_C \\ Y_C \\ Z_C \\ 1 \end{bmatrix} \quad C = \left[\begin{array}{c|c} R_C & \vec{t_C} \\ \hline \bar{0} & 1 \end{array}\right]$$

The matrix R_C and the vertical vector t_C are also a rotation matrix of three degrees of freedom (three angles) and a translation vector of three degrees of freedom respectively, of course, both are also parametric. C is a six degrees of freedom matrix but, unlike T_{6dof3D}, this one represents the transformation of the point cloud from *world coordinates* into *camera coordinates*. λ represents the depth value of the projected

point and it is distinguished in such a way because all values must be divided by it as the last part of the projection procedure, this is usually referred to as *perspective divide*.

In the pinhole-camera model, we assume that the camera is aligned with the Z axis and that it is facing towards $+Z$. Screen borders are also aligned to the XY axis. Usually, if we express the resulting image as a matrix, the first axis (axis of the is), would be aligned to $+Y$ while the second axis (axis of the js) would be aligned to $+X$. Therefore, when we develop the matrix C, we must take this details into account so that the camera is facing towards the parts of the scene that we are interested in.

3.2 Direct methods

Before any definition is given, some concepts are going to be settled. In the image registration context, we will refer to the target image as *template* or *reference image* whereas the image that we iteratively transform until we find a match with the template is referred as the *input image*.

Direct methods attempt to transform the input image into the template image so that we can compute an estimation of the transformation that converts one image into the other image. This can be used for various purposes. In our case, we want to know the motion of our target. In particular, in the three dimensional case, we are going to use point clouds and we want to know the motion of the entire point cloud assuming that the camera is fixed or, alternatively, treat the point cloud as if it was fixed and know the motion of our camera. This double and relative interpretation of the problem is going to be referred in this document as *duality*.

Before the description of the main algorithms that are used in this document, some requirements and more definitions must be introduced. The notation employed in

the development of the explanations in this section is going to be similar to the notation from the thesis [1] and the related article [35].

First, a clear definition of our image registration problem is provided. We start with a couple of intuitive counterexamples. In these problems we do not change the original colors of the input image or those of the template image. We will also preserve the structure of the neighborhoods between transformed points in the original images. This means that the corresponding points match if the colors match. Formally, the *Brightness Constancy Assumption* is introduced as the main requirement in image registration. The BCA is defined as

$$I(f(x,\mu),t) = T(x), \forall x \in \mathcal{V} \subset \mathcal{D} \tag{3.7}$$

where $I(x',t)$ is the input image evaluated at the point $x' = f(x,\mu) \in \mathcal{V}' \subset \mathcal{D}$ and at time t, $f(x,\mu) : \mathcal{D} \times \mathbb{R}^p \to \mathcal{D}$ is the *warping function* (transformation function) which applies the warp described by μ with p parameters to the initial point x and $T(x)$ is the template image evaluated at x. $\mathcal{V}$ and $\mathcal{V}'$ are arbitrary sets of points that must be within the function domain $\mathcal{D}$.

In general, all direct methods in image registration require a series of common steps. They require dissimilarity measure, dissimilarity linearization, search direction computation and parameter and image update steps. All of them also perform a convergence check so that the algorithm is stopped when certain criteria is met. There are multiple ways to define such criteria, however, in this document, only the one that is chosen for the experiments is presented.

The convergence criteria or, to be more precise, the *halting criterion* is a fixed threshold for the step increment (δps in the following formulas) norm. If this norm is greater than a threshold, the algorithm is stopped and the test is considered as *divergent*. If the norm is smaller than another threshold, the algorithm is also

stopped and the test is considered as *convergent*. Additionally if a fixed amount of iterations is surpassed, the algorithm is stopped but no conclusions are derived.

The algorithms that have been chosen to solve the image registration problem are the Lucas-Kanade algorithm [9] and the Inverse Compositional algorithm [13, 14]. We will refer to them therefore as LK and IC respectively for the rest of the document.

3.2.1 Lucas-Kanade

The first algorithm that is going to be described here is the Lucas-Kanade algorithm. It is a forward additive direct method and it is based on the Gauss-Newton optimization scheme. The dissimilarity measure that is used in this algorithm is the squared *residual*. The residual is the dissimilarity between the input image and the template image and is defined as $r(\mu) \equiv T(x) - I(f(x,\mu), t+1)$[1]. The corresponding dissimilarity linearization would then be

$$r(\mu + \delta\mu) \simeq \mathcal{L}(\delta\mu) \equiv r(\mu) + r'(\mu)\,\delta\mu = r(\mu) + J(\mu)\,\delta\mu \tag{3.8}$$

where $J(\mu) \equiv -\left.\dfrac{\partial I(f(x,\hat{\mu}), t+1)}{\partial \hat{\mu}}\right|_{\hat{\mu}=\mu}$ is known as the *Jacobian* of the warped image $I(f(x,\hat{\mu}), t+1)$ evaluated at μ. The parameter increment $\delta\mu$ is used in every iteration to update the parameters additively as follows $\mu' = \mu + \delta\mu$. This linearization follows the Newton minimization method and as such, to perform the linearization, a first order Taylor series is required to locally estimate the parameters of the warp at each step. In the Newton minimization method we would find x_n in $0 = f(x_{n-1}) + f'(x_{n-1})\,(x_n - x_{n-1})$. In this case, we find $\delta\mu$ in our dissimilarity measure which is

[1] $r(\mu)$ depends also on other parameters such as x or t but these are initialized once and are regarded as constants throughout the whole algorithm so there is no need to parameterize those.

$(r(\mu+\delta\mu))^2 \simeq (\mathcal{L}(\delta\mu))^2$.

$$\begin{aligned} 0 = \frac{\partial(\mathcal{L}(\delta\mu))^2}{\partial\delta\mu} = 2\,(r(\mu)+J(\mu)\,\delta\mu)\,J(\mu) = 2\,r(\mu)\,J(\mu)+2\,J(\mu)^2\,\delta\mu \Rightarrow \\ \Rightarrow 0 = r(\mu)\,J(\mu)+J(\mu)^2\,\delta\mu \Rightarrow \delta\mu = \frac{-r(\mu)\,J(\mu)}{J(\mu)^2} = \frac{-r(\mu)}{J(\mu)} \end{aligned} \tag{3.9}$$

This is the definition for a point per point and parameter per parameter basis since x is a single sample point, we are assuming that the images I and T are functions that are defined similarly to the definition 3.3.

To extend this to a finite set of sample points, some modifications must be done. We start with $x \in \mathcal{V}$ which we can rewrite in matrix form[2] for a vector of points $X = (x_1, x_2, \dots x_N)$ where $x_i \in \mathcal{V} \quad \forall i \in 0, 1, 2, \dots N$. This form is also required if there are multiple parameters in the vector μ. We will assume that $|\mathcal{V}| = N$; that $I(X, t+1)$, $T(X)$, $r(\mu)$ and subsequently $\mathcal{L}(\delta\mu)$ are matrices of $N \times 1$ for an arbitrary set of given points X; that μ and $\delta\mu$ are matrices of $n \times 1$ where n is the amount of parameters; and that $J(\mu)$ is a matrix of $N \times n$ where each row corresponds with the derivatives of each parameter at each point of X and in the same order. Only the definitions that change will be shown, the others remain the same.

$$\begin{aligned} (r(\mu+\delta\mu))^2 \simeq \mathcal{L}(\delta\mu)^T\,\mathcal{L}(\delta\mu) \Rightarrow \\ 0 = \nabla_{\delta\mu}(\mathcal{L}(\delta\mu)^T\,\mathcal{L}(\delta\mu)) = 2\,J(\mu)^T\,(r(\mu)+J(\mu)\,\delta\mu) = \\ = 2\,J(\mu)^T\,r(\mu)+2\,J(\mu)^T\,J(\mu)\,\delta\mu \Leftrightarrow \\ \Leftrightarrow 0 = J(\mu)^T\,r(\mu)+J(\mu)^T\,J(\mu)\,\delta\mu \Leftrightarrow \\ \Leftrightarrow \delta\mu = (J(\mu)^T\,J(\mu))^{-1}\,J(\mu)^T\,(-r(\mu)) \end{aligned} \tag{3.10}$$

The matrix product $(J(\mu)^T\,J(\mu))^{-1}\,J(\mu)^T$ is known as the pseudoinverse-Hessian matrix since the product $(J(\mu)^T\,J(\mu))^{-1}$ shares similarities to the actual Hessian

[2] Actually, we can always write this in matricial form but the matrices would be infinite in the same way as the set. If the set is finite, the matrices can be finite.

matrix (second order derivative in matrix form). The explanation can be found in the appendix section of the article [14]. The algorithm can be summarized in the steps shown in the algorithm figure 3.1.

Algorithm 3.1: LK algorithm summary

On-line: Let $\mu_i = \mu_0$ be the parameter initialization
while *halting criteria not satisfied* **do**
    Residual calculation at $r(\mu_i)$
    Jacobian calculation at $J(\mu_i)$
    Calculate search direction using either 3.9 or 3.10
    Update parameters additively using $\mu_{i+1} = \mu_i + \delta\mu$
end

3.2.2 Inverse Compositional

The Inverse Compositional method has almost the same core steps but there are several important differences. The IC is inverse, which means that the search of parameters is performed backwards, so instead of defining the Jacobian in terms of the input image, it is defined in terms of the template image. The IC is compositional, which means that instead of performing the parameter update in an additive fashion, it composes the resulting warps (function composition). This makes the IC an efficient algorithm in terms of performance because the Jacobian can be calculated only once as the template image does not change between different iterations. The algorithm also uses the squared residual as the dissimilarity measure as in LK (3.2.1). The other differences are now presented formally.

In IC the residual has to be defined differently since this algorithm uses an inverse strategy, $r(\mu) \equiv T(f(x,\mu)) - I(f(x,\mu_{\text{accum}}), t+1)$ where μ_{accum} is the accumulated warp and therefore, it is a transformation and not a vector of parameters or a parameter. Since this is an inverse approach, all the local minimizations are performed

backwards (from the T to I), the linearization is performed over $\mu = 0$ instead of any μ entailing

$$r(0 + \delta\mu) \simeq \mathcal{L}(\delta\mu) \equiv r(0) + r'(0)\,\delta\mu = r(0) + J(0)\,\delta\mu \tag{3.11}$$

where $J(0) \equiv \left.\dfrac{\partial T(f(x,\hat{\mu}), t+1)}{\partial\hat{\mu}}\right|_{\hat{\mu}=0}$ and $r(0)$ can be obtained substituting in the new definition of r.

In LK the accumulation was done additively whereas in IC the accumulation is performed compositionally like $\mu' = \mu \circ w(\delta\mu)^{-1}$ where μ' is the last accumulated warp w is a function that transforms the vector of parameters to a warp. Those are the main formal differences required to analytically differentiate the correct formulas in IC since the process is exactly the same as in LK.

The process of finding $\delta\mu$ in IC is the same as in LK both in the single point and parameter form and the matrix form so for the sake of space both results will be enumerated here.

$$\text{Single parameter:} \quad 0 = \frac{\partial(\mathcal{L}(\delta\mu))^2}{\partial\delta\mu} \Leftrightarrow \delta\mu = \frac{-r(0)}{J(0)} \tag{3.12}$$

$$\text{Matrix form:} \quad 0 = \nabla_{\delta\mu}(\mathcal{L}(\delta\mu)^T\,\mathcal{L}(\delta\mu)) \Leftrightarrow \delta\mu = (J(0)^T\,J(0))^{-1}\,J(0)^T\,(-r(0)) \tag{3.13}$$

The algorithm is indicated in figure 3.2.

In order for the IC to converge and exploit its efficiency, some extra conditions must be met apart from the BCA. We say that these methods are efficient if the convergence behavior is good in general terms. The formal definitions of these requirements are available in the article [35]. These conditions are basically summarized in the called *Extended Brightness Constancy Assumption* which also imposes the brightness assumption in the Jacobian of the images.

Algorithm 3.2: IC algorithm summary

Off-line: Jacobian calculation at $J(0)$
On-line: Let $\mu_i = w(\mu_0)$ be the warp initialization
while *halting criteria not satisfied* **do**
    Residual calculation at $r(\mu_i)$
    Calculate search direction using either 3.12 or 3.13
    Update warp compositionally using $\mu_{i+1} = \mu_i \circ w(\delta\mu)^{-1}$
end

Formally these requirements can be expressed as

$$\begin{aligned} \text{BCA:} \quad & I(f(X,\mu),t) = T(X) \quad \text{(formula 3.7 and } X = \mathcal{V}) \\ \text{EBCA:} \quad & \text{BCA and } X = g(X', \phi_0 + \Delta\phi) \Rightarrow \\ \Rightarrow \quad & I(f(g(X', \phi_0 + \Delta\phi)) = T(g(X', \phi_0 + \Delta\phi)) \end{aligned} \tag{3.14}$$

where $X \in \mathcal{D}$ and $X' \in \mathcal{D}$ are sets of points and f and g are warps and ϕ_0 is a vector of parameters and $\Delta\phi$ is a small increment of this vector.

The EBCA implies that the brightness constancy must be also maintained over a composition of warps (requirement 1) with a small increment (requirement 2) which is equivalent to saying that it has to be maintained in the Jacobian of the input images and the template image. In the original article, these requirements are referred to as *parameter equivalence* and *parameter independence* respectively. If the reader seeks further understanding of the theory behind the EBCA and its implications and the results in various experiments, all the information is carefully presented in [35]. The theory of the EBCA is in section 4 and the experiments are in section 5.

3.2.3 Other notable mentions

There are other important variants of direct methods that are worth mentioning in the topic. These techniques are not going to be explained in detail since they are not going to be used in the rest of the document unlike LK or IC and they are well explained in their respective articles.

The first approach worth mentioning is *Hager-Belhumeur* [10] algorithm which is a variant of LK. It is an additive approach that attempts to reduce the computational costs of it. The latter performs many computations in every iteration since it has to recalculate the Jacobian at every step (see the step calculation formula of $\delta\mu$ at 3.10). Hager-Belhumeur reduces the computational time using the derivatives of the template image in the gradient calculation and performing a factorization of the Jacobian matrix so that at least one part can be computed off-line (this part also includes the gradient image of the template).

The second and last approach is the *Forward-Compositional* [11, 12] algorithm which is a compositional algorithm. The procedure is very similar to the IC as well as the resulting formulas required for each step. The main difference is that all the calculations of the Jacobian are made over the input images instead of the template image. This implies that the Forward-Compositional algorithm is far slower than its inverse since it has to recalculate the Jacobian at every iteration as the input images also change between iterations.

3.2.4 Additional improvements

Apart from these algorithms and their variants, there are several improvements that can be applied to them depending on the case. These improvements are changes to parts of the previous algorithms that attempt to address certain problems these algorithms present in certain cases.

For example, we may want to use an algorithm such as LK for its compatibility reasons but we may also need computation performance offered by algorithms such as IC. In case we want to improve the performance of any algorithm, *pixel selection* techniques can serve that purpose. And if we want to improve the convergence, we may consider using *coarse-to-fine schemes*.

The objective in pixel selection is to reduce the amount of pixels to be processed from the original images. This can improve two aspects of the main algorithm. As mentioned before, pixel selection can improve performance and this is understandable since the matrices that we are going to work with after pixel selection are obviously going to be of smaller or equal size as the original. But it can also have another desirable effect over the algorithm. If pixel selection is able to determine which pixels are not appropriate to achieve convergence in the algorithm because these pixels are either uninformative in comparison to others or they contradict the gradient given by other pixels (nullifying the final gradient result), these pixels can be removed to aid the main algorithm in the residual minimization. So the benefits provided by this technique may be twofold.

In coarse-to-fine selection schemes the strategy is to accelerate convergence reducing the resolution and also smoothing the image since it is known that smoother images have better convergence. This is achieved using what is called a pyramid [36] of images where each layer of the pyramid is a lower-resolution version of the original images with a low-pass filter such as the Gaussian filter. The minimization process starts at the lowest resolution until convergence is achieved. Then the algorithm changes the images to others of higher resolution (next layer) and starts to iterate using the direct image alignment algorithm again at the previous parameter results (change of the algorithm initialization). This process is repeated until all the layers of the pyramid have been used and, in theory, a greater degree of convergence is achieved. In the literature, the algorithm is usually referred as "multi-resolution"

as well. These are several references were the last two algorithms is employed [23–29, 37]. An example of coarse-to-fine scheme applied on a single image, see figure 3.2.

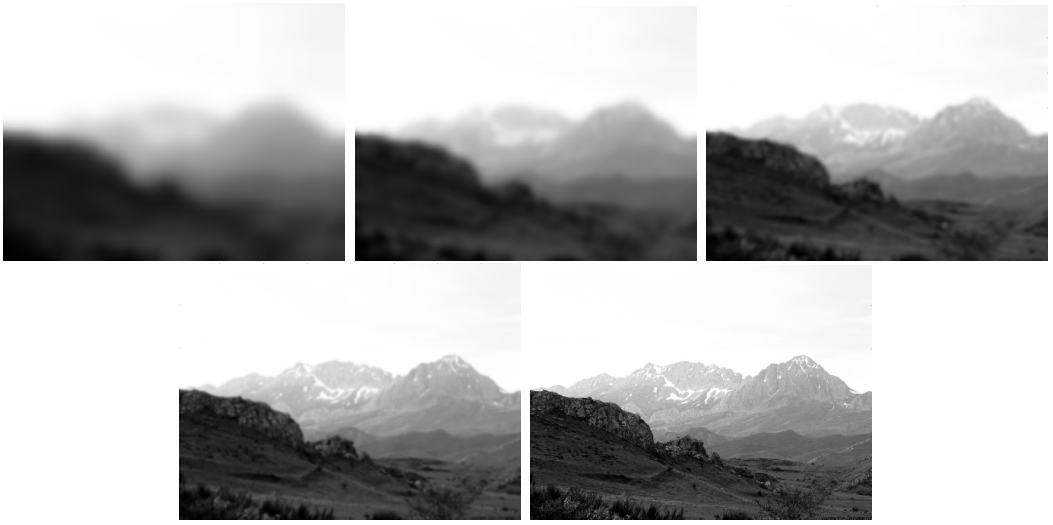

FIGURE 3.2: Several layers of the pyramid in a coarse-to-fine scheme.

Other strategies may not attempt to reduce the amount of pixels directly but instead they attempt to improve the robustness and accuracy of the algorithm in cases that certain parts of the images are not reliable for image registration. This is referred to as *robust estimation*. Those parts are usually considered outliers for the algorithm since they are those that decrease reduce convergence. This is actually very similar to pixel selection but it does not reduce the amount of pixels in images. This technique uses the residual as the guide to know how much do we have to rely on each pixel's information. This reliance is provided as a diagonal matrix that is calculated directly from the residual and a chosen robust M-estimator [26, 38] and, following our previous notation, it can be formalized as

$$\mathcal{O}(x) = \rho\left(\sum_{x\in\mathcal{V}} r(x)\right) \tag{3.15}$$

where ρ is our estimation function and $\mathcal{O}$ is the final estimated value for each point x. Depending on the way we formalized the direct method, we may obtain different formulas for each step and different precomputations. For the sake of clarity, we show how is this applied to LK. If we take the resulting parameter update formula 3.10, we can derive the following formula (based on [26]) with the robustness estimation capability

$$\delta\mu = (D\ J)^{+}\ D\ (-r(\mu)) \tag{3.16}$$

where $(D\ J)^{+}$ is the pseudo-inverse matrix of $D \cdot J$. This diagonal matrix serves as a series of weights for each pixel so that the more reliable a pixel is, the higher the weight is and, consequently, the more it influences in the final result of the minimization step. In the previous formula it can be seen that the matrix product and the pseudo-inverse must be calculated each iteration and, henceforth, it is not beneficial for algorithms such as the IC because the reason behind their existence is the attempt to reduce the amount of calculations.

3.3 RGB-D cameras

In this section, a brief introduction to the various RGB-D cameras is presented to give the reader a brief notion of how are these images usually generated. We can divide current depth sensing techniques into three different categories [39]:

- **Interferometry**: based on the measurements made over the amount of interference between monochromatic waves. This technique is very precise in short distances ranging from micrometers to centimeters.
- **Triangulation**: these try to measure depth using the virtual triangle that is formed between the lines of sight of an optical system and a point in the scene.

- **Time of Flight**: these perform measurements of the time-of-flight of signals emitted from the source of the camera to a point in the scene that subsequently collides and bounces back to the camera receiver. Typically, the most popular techniques in ToF are those based on *Continuous Wave Modulation* and those based on *Photometric Mixer Device* ToF. In these cases, the phase shift difference between the emitted and received signal is measured to calculate the distance (depth).

In triangulation, there are essentially two main trends depending on how is the triangulation performed. The triangulation can be performed *actively* or *passively*.

When we perform passive triangulation, our optical system is made of several (at least two) cameras that serve as *stereo* vision. The procedure to perform triangulation is passive since correspondences of points in the scene seen from various cameras have to be found. Once a match is found for every pixel in the image obtained from each camera (or at least, some pixels), triangulation can be performed unless those cameras are aligned with a given point in the images. Thus, the triangle must have an area different from zero.

If active triangulation is performed, the optical system has light sources instead of various cameras (only a single camera is needed). This greatly improves the matching task since each point can be emitted from the light source in the desired direction. The camera must find how is the scene modifying the emitted ray in order to calculate the distance via triangulation. For a single distance measurement, this is trivial since there is only going to be one point of emitted light and the camera is going to perceive the reflected light at the expected position or relatively close to it. However, if several distances are meant to be calculated, for instance, the distance of each pixel in the camera, it is necessary to perform one calculation at a time. With the appearance of Kinect sensors and its derivative, this is no longer a problem. The Kinect sensor is an example of active triangulation using an emitted

light-pattern that is known a priori and the deformations of this pattern provide the depth information via triangulation. The only drawback is that the pattern cannot provide good accuracy in camera space unless greater camera resolution is provided to the system. This would require a faster processor and it would be more expensive not only because of the processor but also because of the greater camera resolution and light emitter resolution. The instructions to setup a Kinect sensor are provided in the appendix A.

Chapter 4

Methodology

This chapter serves as a farther explanation of the implementation details of LK and IC, especially those related to the Jacobian calculation and the procedure to adapt LK and IC to RGB-D based images.

4.1 The unidimensional case

To start understanding the behavior of any sort of direct method (in general, all those derived from LK, see 3.2.1), one-dimensional examples may serve better for introductory purposes.

To simplify our examples and assure convergence, the BCA (see definition 3.7) must be satisfied. In one-dimensional examples, any simple continuous function can satisfy it. These simple continuous functions will serve as the equivalent to the template and input images that were explained in chapter 3. In the following examples, the function g will serve as the equivalent of the template image (in this case is the target shape of our function) and f will be the equivalent of the input image which

in principle is the same as g (if it was not, it would not satisfy the BCA) but it is affected by an offset transformation. The transformation must satisfy BCA conditions as well.

For example, we choose a simple unidimensional continuous function such as a Gaussian function defined as $\mathcal{G}(x) = \frac{1}{\sqrt{2\,\pi\,\sigma^2}} \exp\left(-\frac{(x-\mu)^2}{2\,\sigma^2}\right)$ and we perform a simple transformation. The simple transformation will be an offset (also known as translation or commonly as a shift) in parameter μ since it establishes where is the median in the Gaussian distribution function and, therefore, it shifts all the function in the x variable axis.

To illustrate this, the reader can see figure 4.1 which shows two Gaussian functions. Function g is centered at $\mu = 1$ while function f is centered at $\mu = 0$. The surfaces associated to the residuals (see 3.2 to understand what the *residual* is) and their derivatives with different parameters are also provided in figure 4.2. The derivatives are, of course, what we have been calling the Jacobian (see 3.2 as well if needed).

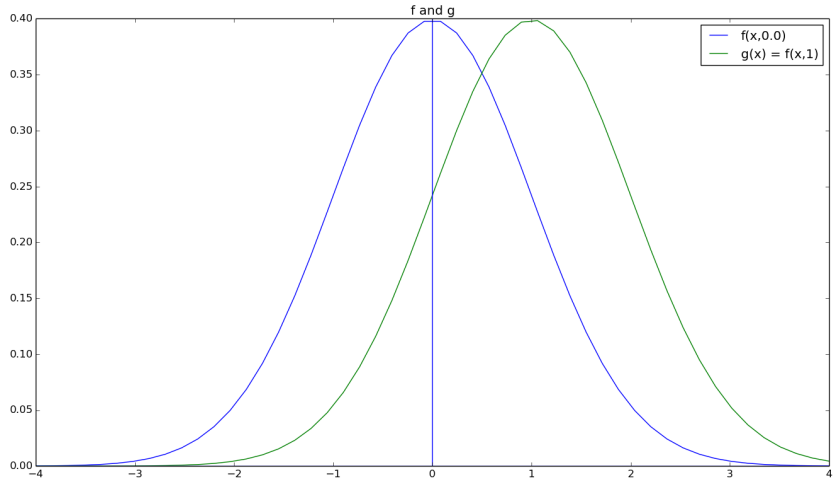

FIGURE 4.1: Function g is centered at 1 while function f is centered at 0.

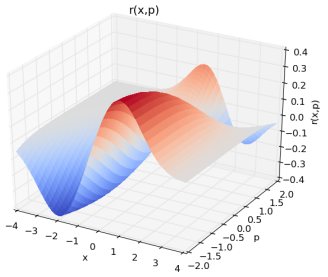

(A) Residual

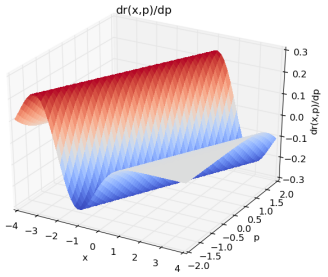

(B) Residual derivative

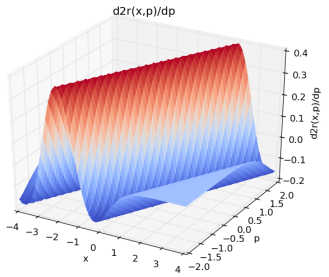

(C) Residual second derivative given just to understand the function's behavior

FIGURE 4.2: Residual and its derivatives depending on the parameter μ which is renamed in the axis as p

The residual surfaces in 4.2 show that the residual r changes as the parameter μ changes. In the first surface, it can be seen that the difference between f and g is smaller as the μ of f gets closer to the μ of g. This is especially notable when both f and g match each other and the surface is flat. This happens when $\mu = 1$ as expected.

If we perform a Newton optimisation we can iterate over $f(x, \mu)$ until $\mu \approx 1$. The Newton method applies to a single starting point rather than a set or vector of points and in our case the minimization is done over a set of sampled points (in figure 4.1

we are working with the (-4,4) range of values as the graph shows). We need then the matrix form to be able to work with this set of points which is equivalent to using the Gauss-Newton method as seen in section 3.2.1. In this example, we perform this optimisation step over μ using the LK algorithm (see 3.1).

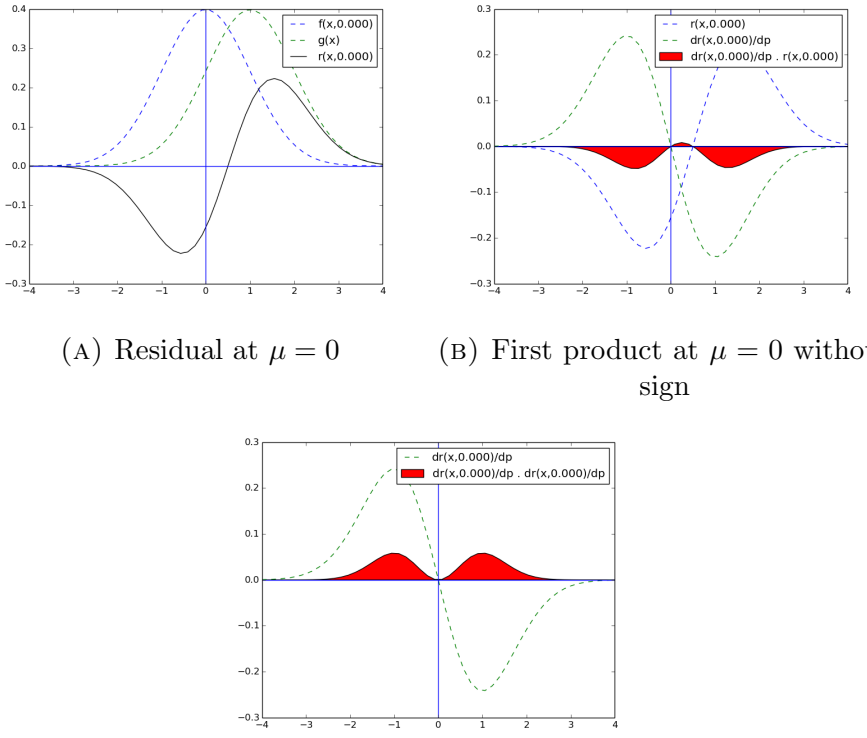

(A) Residual at $\mu = 0$

(B) First product at $\mu = 0$ without sign

(C) Second product (pseudo-inverse) at $\mu = 0$

FIGURE 4.3: First iteration of the optimisation

In each iteration, the graphs show the product to obtain each increment $\delta\mu$ divided into two parts. The first part of the product in equation 3.10 is $(-J(\mu)^T r(\mu))$ where J and r are sampled at every point of the set. With a single parameter, this can be graphically illustrated as the area under the curve of these products (colored in red in figure 4.3) if we had an infinite amount of sample points. In these examples, it is not exactly the area but for the sake of clarity, the area will be used to show

the behavior of the LK algorithm since it is more intuitive graphically[1]. The second product is the one related to the pseudo-inverse matrix $(J(\mu)^T\ J(\mu))^{-1}$. This one can also be regarded as the area under the curve but with the inverse effect on $\delta\mu$.

This implies that for the first part, the larger the area under the curve, the larger the value that will result in $\delta\mu$ for the following iteration and with opposite sign because of the minus. Note that this area can be positive or negative. However, the second part has the inverse behavior, meaning that the larger the area under the curve, the smaller $\delta\mu$ will be. Also note that this area cannot ever be negative since the square of any number or in particular, the square of the Jacobian, cannot be negative by the definition of a square operation in a matrix.

The first iteration (figure 4.3) leads clearly towards a greater value of μ because of the larger negative area against the positive area of the first product, then the sign is inverted leading to a positive value. The second product is large enough to make the final value to be relatively lower. This is a desired effect since the closer we are to the result, the smaller we want the steps to be.

The following two iterations (figures 4.4 and 4.5) show that there is a clear convergence and in the last iteration the area of the first product is almost invisible. The algorithm converges with $\mu = 0.999999994936$ just using a halting criterion of a minimum norm of 0.1 per increment.

Since our direct methods rely on local optimisations and, consequently, on the initialization parameters, these are essential for the convergence of the algorithm. Because of their nature, these algorithms can converge to local optima and this is unavoidable if the source of data is ambiguous. In our unidimensional example we can create a f function that instead one Gaussian distribution, it has two Gaussian distributions sufficiently separated. If the initialization is done in such a way that one of the

[1] Actually it is just the height at each sampled point rather than the area. It would be the area if there was an infinite amount of points.

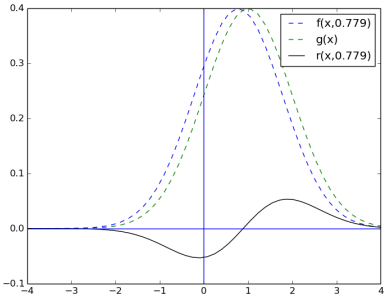

(A) Residual at $\mu = 0.779$

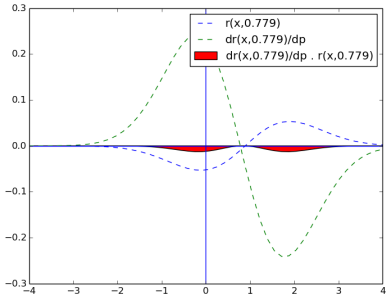

(B) First product at $\mu = 0.779$ without sign

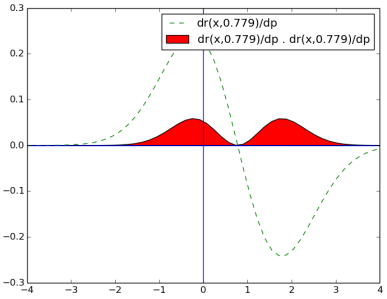

(C) Second product (pseudo-inverse) at $\mu = 0.779$

FIGURE 4.4: Second iteration of the optimisation

Gaussian distributions in f matches the other Gaussian distribution in g but that does not happen for the other pair of Gaussian peaks, the wrong peak is matched and convergence will most likely be reached immediately towards the local optima. But this is not the only drawback that we can find in locally-based algorithms. Convergence can also be impossible to achieve if f and g are not sufficiently close even without any sort of global ambiguities. To show this, another example is proposed that is directly derived from the previous one.

The example in figure 4.6 shows a case where, according to the algorithm, convergence is achieved in the first iteration using the 0.1 norm threshold as we did before.

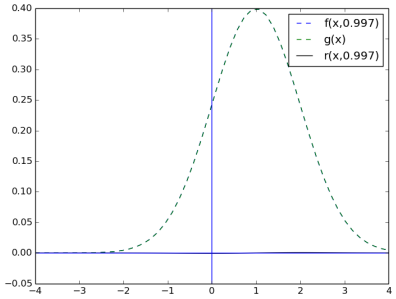

(A) Residual at $\mu = 0.997$

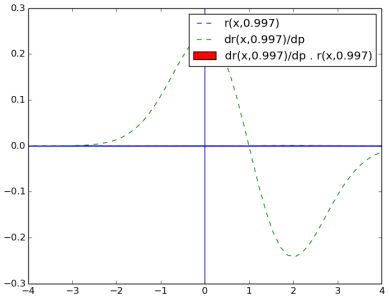

(B) First product at $\mu = 0.997$ without sign

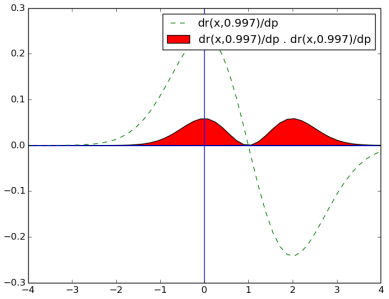

(C) Second product (pseudo-inverse) at $\mu = 0.997$

FIGURE 4.5: Third iteration of the optimisation

This shows that, in this variant, the algorithm cannot decide how to choose the next parameter increment since the data is not good enough. If the threshold is changed from 0.1 to 0.001, the algorithm keeps slowly iterating until it gets to the destination due to the fact that Gaussian distributions are always above zero and their derivative is never zero in $\mathbb{R}$. If we use a different function were the derivatives and the residual do not aid at all, convergence will be impossible regardless of the

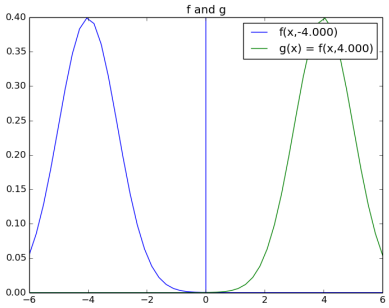

(A) f and g at $\mu = -4$

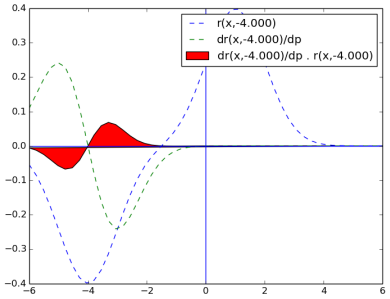

(B) First product at $\mu = -4$ without sign

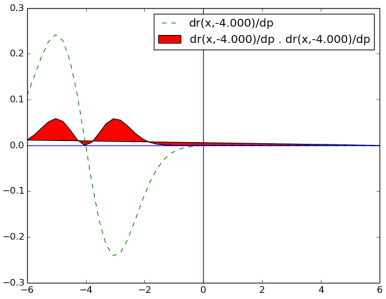

(C) Second product (pseudo-inverse) at $\mu = -4$[a]

[a] In this graph there is a representation error due to Matplotlib's filling algorithm, the area should be filled from the axis but they use the enclosed polygon instead.

FIGURE 4.6: Example of slow convergence

chosen threshold. Functions like the following can be used to cause such problems

$$f(x,\mu) = \begin{cases} 0 & \text{if } x \in (-\infty, -1+\mu] \\ \dfrac{\cos(\pi(x-\mu))}{2} + 0.5 & \text{if } x \in (-1+\mu, 1+\mu] \\ 0 & \text{if } x \in (1+\mu, \infty) \end{cases} \tag{4.1}$$

This case is also illustrated in another figure 4.7. Convergence is eventually achieved in the implementation of this example using a very low threshold, but this is due to the lack of samples (50 samples in the x axis for all these examples) which provides some noise that can help in the convergence eventually though it is unlikely. And the more samples are used for this test, the worse the convergence is[2].

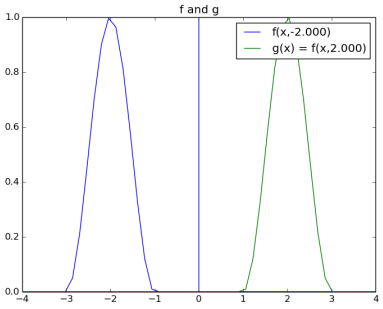

(A) f and g at $\mu = -2$

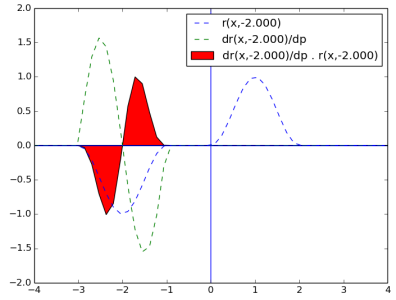

(B) First product at $\mu = -2$ without sign

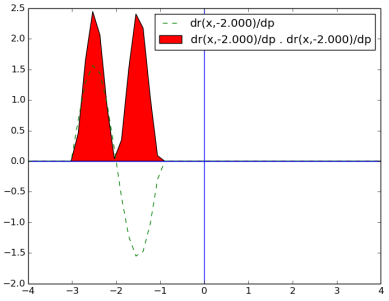

(C) Second product (pseudo-inverse) at $\mu = -2$

FIGURE 4.7: Example of no convergence

Hopefully, these simple examples illustrate how LK works for a single parameter (unidimensional optimisation). From now on, any arbitrary amount of parameters

[2]This has been also tested using 1000 samples and the convergence is several times lower than before. This has not been chosen at first so that these strange cases could arise so that a better observation is made.

will be used in the examples and reasoning. Next sections will not be as rich in detailed examples since it will be assumed that the basic understanding process has already been completed by the reader after reading these experiments.

4.2 Implementation details

This section presents some details of the implementation that have been used throughout this document to perform the experiments. If no comments are made about a certain detail of LK or IC or any definition provided in chapter 3, it means that the exact definitions available in that chapter are used. Advantages and disadvantages of each implementation choice are also discussed in this section.

4.2.1 Jacobian calculation

Probably, the most important choice while implementing either LK or IC is how to calculate the Jacobian matrix. The Jacobian matrix is the core of both algorithms and also of other variants like those presented in section 3.2.3 or those cited in the literature review at 2.4.

The Jacobian matrix influences in the final increment value of each iteration in a very meaningful way since it affects the pseudo-inverse as we have seen in previous section 4.1 and also in the original formulas from sections 3.2.1 and 3.2.2. The Jacobian matrix can be calculated in many different ways and the technique used is entirely the implementer's choice, yet, it is crucial that the chosen implementation is equivalent to the definitions established in those sections. If the definitions are not met, it is likely that the algorithms will not perform well in practice.

In this document, two possible implementations (and some other hybrids) for the Jacobian in LK and in IC are discussed: the analytic Jacobian and the numeric Jacobian.

4.2.1.1 Analytic Jacobian

The analytic Jacobian follows the idea proposed in [14] which was probably derived from the various proposals in [10]. In [14], the Jacobian is known as the *steepest-descent images* and is calculated by dividing the Jacobian formula from 3.2.1 into several parts:

$$J(\mu) \equiv -\frac{\partial I(f(x,\hat{\mu}),t+1)}{\partial \hat{\mu}}\bigg|_{\hat{\mu}=\mu} = -\frac{\partial I(f(x,\hat{\mu})),t+1)}{\partial f}\,\frac{\partial f(x,\hat{\mu})}{\partial \hat{\mu}}\bigg|_{\hat{\mu}=\mu} \tag{4.2}$$

In [14], they use W to refer to f as a matrix-based transformation and p instead of $\hat{\mu}$ to refer to the variable(s) related to the parameter(s) to be minimized. This separates the Jacobian calculation into two different calculations. The first one is the calculation of the gradient images of I at each iteration which is shown in the article as ∇I. Nevertheless, the reader must note that there is a spelling mistake (or rather a notation mistake) in this article related to ∇I. In figure 1, they explain all the steps in LK done in an analytic way and step 3 states that the implementer has to

> "Warp the gradient ∇I with $W(x;p)$"

This can be misleading since the gradient operation must be performed **after** I is warped with $f(x,\mu)$ and this is actually crucial. If done incorrectly, the Jacobian formula 4.2 does not hold and unexpected behavior will result.

After performing the gradient operation of the warped image, the derivatives of the warping function f must also be calculated. These derivatives depend on the warp

that is going to be used during the process. For example, the derivatives of an affine warp in 2D and in matrix form are

$$\frac{\partial f(\vec{x},\mu)}{\partial \mu} = \left(\begin{bmatrix} x & 0 & y & 0 & 1 & 0 \\ 0 & x & 0 & y & 0 & 1 \end{bmatrix} (x,y) \right) \cdot \vec{x} \tag{4.3}$$

as shown in [14]. This article offers other derivatives for other transformations as well.

In the IC algorithm, the same can be done using the formulas discussed in section 3.2.2.

$$J(0) \equiv \left. \frac{\partial T(f(x,\hat{\mu}),t+1)}{\partial \hat{\mu}} \right|_{\hat{\mu}=0} = \left. \frac{\partial T(f(x,\hat{\mu}),t+1)}{\partial f} \frac{\partial f(x,\hat{\mu})}{\partial \hat{\mu}} \right|_{\hat{\mu}=0} \tag{4.4}$$

The calculation process in practice is shown in figure 4.9 where *gx* and *gy* are the respective gradients in both axis and *Jxp1* and *Jyp1* are the analytic derivatives of the warping function (in *Jxp1* black is -1, grey is 0 and white is 1). The gradients and the Jacobians are multiplied per-pixel in the same axis where the result of each product are the two images on the right. These images are added per-pixel giving the final Jacobian which is the one that appears with the label *Jp1*.

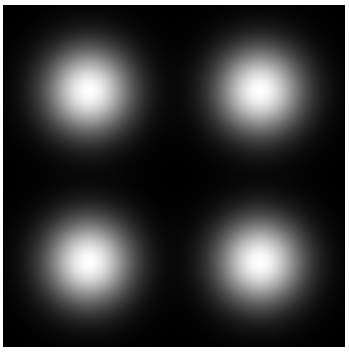

FIGURE 4.8: Texture image used in figure 4.9 (4 Gaussian distributions in 2D).

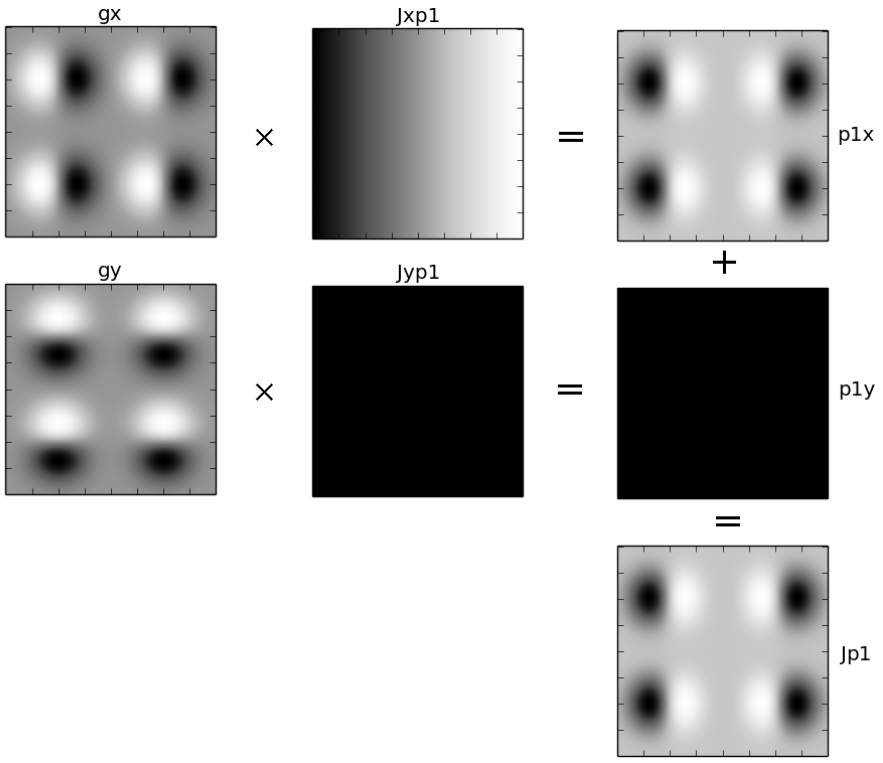

FIGURE 4.9: Analytic Jacobian in one parameter generated in various steps. p1 is the actual Jacobian.

Both LK and IC require the calculation of the gradient images ∇I and the calculation of the warp derivatives $\dfrac{\partial f(x,\mu)}{\partial \mu}$. The gradient images have to be calculated over discrete sets of sample points since after warping (and also before) the transformed image is also made of pixels which by nature are discrete and finite (this has already been discussed in section 3.1.1)). To perform these derivatives images must be treated as if they were continuous functions, so a special procedure is required. There are various ways to calculate this:

- **Derivative definition**: using the general definition of derivation[3], we can calculate the derivatives per pixel in one axis. This can be applied performing

[3]The definition that is referred to is $f'(x) = \dfrac{f(x+\alpha) - f(x-\alpha)}{2\,\alpha}$

a horizontal or vertical convolution with a kernel $K = [-1\ 0\ 1]^T$ or $K = [-1\ 1]^T$. This definition is suitable in general but it does not take into account neighboring pixels others than those aligned with the current pixel in the current axis.

- **Sobel filter**: the Sobel filter can be applied to create gradient images. This filter does take into account all 8 neighboring pixels of the current pixel since it performs a convolution with a kernel of 3×3 which is usually of the form[4]

$$K_{\text{SobelX}} = \begin{bmatrix} -1 & 0 & 1 \\ -2 & 0 & 2 \\ -1 & 0 & 1 \end{bmatrix} \tag{4.5}$$

  For the vertical version, use the transpose matrix K^T_{SobelX}.

- **Scharr filter**: this filter is similar to the Sobel filter since it is also based on a convolution of a 3×3 kernel. This kernel is supposed to yield better results since it resembles more a Gaussian filter.

$$K_{\text{ScharrX}} = \begin{bmatrix} -3 & 0 & 3 \\ -10 & 0 & 10 \\ -3 & 0 & 3 \end{bmatrix} \tag{4.6}$$

The last two techniques are more accurate because they mimic a continuous function where each pixel is a Gaussian distribution with a certain maximum value. It can be imagined as a surface where the heights at each point are the image values and each sampled point is a Gaussian distribution with the median centered at that point.

[4]This kernel and the Scharr kernel are provided in OpenCV and this is the URL where the matrices have been taken from http://docs.opencv.org/modules/imgproc/doc/filtering.html?#sobel (July 2015)

All of these variants provide the gradients over a single axis, so in order to calculate all the gradients in a two-dimensional image, these calculations have to be done twice.

4.2.1.2 Numeric Jacobian

The numeric Jacobian will be divided into various degrees of "numericness". We can calculate numerically various parts of equations 4.2 and 4.4 while calculating analytically other parts. Nevertheless, all these variants are implemented in the same way with minor varying details.

This Jacobian is calculated numerically in the sense that it is calulated performing multiple evaluations of the function to be derivated. The evaluations in the analytic Jacobian are instead done over the derivatives.

This can be done using the same generic derivative definition that we have shown before in this document:

$$f'(x) = \frac{f(x+\alpha) - f(x-\alpha)}{2\,\alpha} \tag{4.7}$$

where α is the offset that we can tweak to change the precision of the estimations.

Then we can apply this definition to those parts that we have already presented in equations 4.2 and 4.4. For instance, if we want to calculate the warp derivatives using a generic estimation rather than the actual derivatives we can do the following

$$\frac{\partial f(x,\mu)}{\partial \mu} = \frac{f(x,\mu+\alpha) - f(x,\mu-\alpha)}{2\,\alpha}, \quad \alpha \to 0 \tag{4.8}$$

for a given point x and parameter μ. This can be calculated for every sample point $x \in \mathcal{V}$ and every parameter $\mu \in \mathcal{P}$. The application of this definition in the gradient has already been provided in the derivation variants.

If we can apply the derivative definition in each part, we can also apply the derivative definition to the whole Jacobian:

$$\text{LK:} \quad -\frac{\partial I(f(x,\mu),t+1)}{\partial \mu} = -\frac{I(f(x,\mu+\alpha),t+1) - I(f(x,\mu-\alpha),t+1)}{2\,\alpha}, \quad \alpha \to 0 \tag{4.9}$$

$$\text{IC:} \quad \frac{\partial T(f(x,\mu),t+1)}{\partial \mu} = \frac{T(f(x,\mu+\alpha),t+1) - T(f(x,\mu-\alpha),t+1)}{2\,\alpha}, \quad \alpha \to 0 \tag{4.10}$$

The definition for IC has been given with a generic μ though in practice, usually $\mu = 0$.

We can even be more generic and apply the definition of the Jacobian. At the beginning of section 3.2.1, a linearization is performed and the derivative of the residual $r'(\mu)$ is renamed as $J(\mu)$. If we follow the definition thoroughly we obtain

$$\frac{\partial r(\mu)}{\partial \mu} = \frac{r(\mu+\alpha) - r(\mu-\alpha)}{2\,\alpha}, \quad \alpha \to 0 \tag{4.11}$$

which is the most generic Jacobian definition that can be applied to LK or IC alike and even for alternative definitions of the residual function r.

4.2.1.3 Comparison of Jacobian calculations

The advantages and disadvantages experienced in both cases will be discussed in this section.

The main remarkable advantages of the analytic calculation of the Jacobian are:

1. All the derivatives of the warp have been calculated analytically off-line and, thus, they do not need to be calculated in real time in every iteration. This means that we can implement these derivatives directly just like if it was a fixed

part of the algorithm with no extra requirements. The only thing that requires a per-case calculation is the gradient of the images since we cannot assume that we know how the input or the template images are. The consequence of these prior calculations are obviously correlated to a better performance because of the lesser amount of calculations.

2. Due to the nature of analytic derivatives, these are theoretically exact as long as a function is derivable in every single point.

In contrast, the main advantages of numeric Jacobians are:

1. Referring to the first point in support of the analytic Jacobian, even though the numeric Jacobian is calculated in real time, it is not always better to have an analytic derivative in terms of computational performance. The reason behind this claim is that analytic derivatives of a function may be much more complex than the original function they came from. If this is the case, the numeric derivative is in a clear advantage since all it requires is the original function and it will cost two evaluations of the function, a subtraction and a division (see formula 4.7). This is of course not trivial and depends on the problem's requirements. One must also take into account the fact that performing a correct image gradient calculation is also something that requires heavy computation (see section 4.2.1.1) though the implementer can easily take advantage of its parallelism.

2. Another disadvantage of the first point is the total lack of flexibility. One implementation will work only for one warp. A second implementation is needed in a second warp. This implies that it goes against the long-term implementation maintenance.

3. Referring to the second point, even though these are exact and even though in the numeric Jacobian the accuracy is controlled via h in formula 4.7, it is not

always trivial to find a continuously derivable function that fits the problem specifications. For example, we may use affine transformations to transform a bidimensional image (see definitions and formulas in 3.1) to another image that looks closer to the virtual camera (basically, we scale the image to make it bigger). This image is unfortunately a discrete function and it can only look smooth in with subpixel precission cases such as this if a filter is applied. If we did this, we would have to include this filter into our calculations since it is part of the transformation and when this happens, the derivatives can start to become overwhelming. The numeric approach needs no additional attention[5]. This is illustrated in figure 4.10.

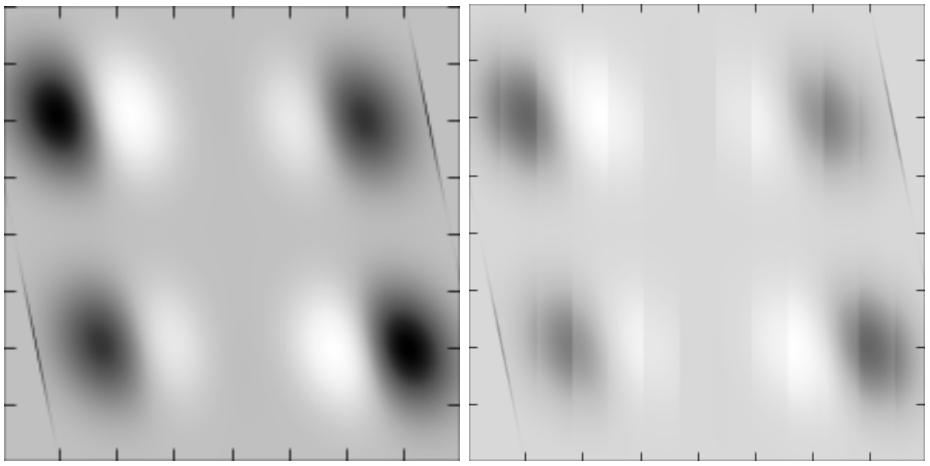

(A) Analytic Jacobian (no artifacts) (B) Numeric Jacobian (with artifacts)

FIGURE 4.10: Differences in practice between the analytic and the numeric Jacobian.

As a result, and after several tests, the numeric approach has been chosen to perform the rest of the tests in this document. We heavily take advantage of the numeric Jacobian implementation's advantages especially those discussed in point 3 because

[5]Note that this is also related to the function complexity that was mentioned in point 1 of the numeric Jacobian advantages.

of our f function requirements in practice (which will be addressed in next section). The next section will refer to how can this implementation be advantageous in RGB-D problems.

4.2.2 RGB-D in direct methods

In this part of the document, details related to the implementation of LK and IC in direct methods is also discussed. However, most of the theory behind the chosen approach to deal with RGB-D based images has already been described in chapter 3, especially in section 3.1.2.

The tests presented in this document are going to be based entirely on *point-clouds*, 3D transformations of 6 degrees of freedom and the *pinhole-camera* model as stated in section 3.1.2. We choose *point-clouds* because it seems to be a simple and plausible standard way to produce 3D samples of any sort of volume, however, several alternatives exist that may be more suitable in other scenarios. The transformation is the one named as $T_{6\text{dof3D}}$ described in section 3.1.2 which will be used in a per-point basis. And, we choose the *pinhole-camera* model for the virtual camera because it is the standard to simulate any real camera and in case these algorithms are applied to real images, the real parameters are required.

To adopt the LK and IC algorithms as direct methods to solve our problem we need to do slight changes to the processes that are already detailed in section 3.2. The transformation function f becomes the function that combines the 3D transformation from 3.4 and the projection from 3.6. Using the same notation, the complete transformation $f : \mathbb{P}^3 \to \mathbb{P}^2$ becomes:

$$f : P \to P_S = \left[\begin{array}{c|c} K & \bar{0} \end{array} \right] \cdot C \cdot T_{6\text{dof3D}} \cdot P \tag{4.12}$$

Since the transformations may include the grey-scale component retrieved from the camera RGB color channels, that also has to be taken into account. But the addition of color into our problem does not require any change in f. Each point will have an associated color value so the only requirement in this case is to be able to track each point during the procedure and to retrieve its color when needed.

In practice, the color values are stored alongside the point-cloud data and these values are retrieved when the perspective projection is done. This idea is the same that is used in [26]. They call it the *extended images* which in practice is the same as the definition that has just been given in the previous paragraph. In this article, they refer instead to two separate images with different meanings, but that is only a definition difference since in practice the effect of the definition given here is the same. Note that treating color alongside depth data as if it was another point means that no preferences or biases are given towards one type of data or the other.

There is an additional problem that has not been addressed in the previous definition of f. Projecting points into the virtual camera plane is needed because we are assuming that we are given two images, thus two planes with color values associated to their coordinates. But our definition 4.12 will cause unnatural incoherences with the behavior that a real projection actually has. The lack of coherence in the definition 4.12 stems from the fact that in reality if two points are aligned with the camera origin, the closest point is the one that is actually projected. If the closest point was transparent, light could pass through it leaving the farthest point partially visible. In our problem definition, we assume that all points occlude other points when these are aligned. Depending on the order we execute our algorithm, some points will stand in front of other points even if these points are not closer. This means that previous definition also requires a check of priorly projected points in the screen or, alternatively, it needs to reorder aligned points (actually, there are more possible alternatives to solve this).

In practice, we project all these points into discrete images and one point may fill up to one pixel once projected. So the only thing left to do is to check if a given pixel of the final image already has a depth value that is lower than the newer value. This task can be considered inside the definition of f or even in the definition of I and T as functions. The image function $\mathcal{I}$ can be seen as the function that iterates over all the transformed points P_S in screen coordinates and that returns the closest point to the camera in the pixel that we are asking for. The resulting algorithm for a single point P assuming that color values are also provided would be the one shown in figure 4.2.

Algorithm 4.1: Projection algorithm in RGB-D

Input: point P from point-cloud and its associated color g in grey-scale
Transform P into P_S using f from definition 4.12
Create temporary space for the warped image I_w
Transform P_S coordinates into discrete pixel coordinates performing a perspective divide P_S/λ (acquire indices (i, j) after this division to access matrix I_w)
if λ *closer than* $I_w(i, j)$ **then**
    Store λ in I_w
    Store g in I_w
    Note: this conditional branch is the only thing that cannot be executed in parallel though it can be executed with certain parallelism for those points that do not lie in the same target pixel.
end

Apart from this procedure, it is also common to fill neighboring pixels as if the current point was actually larger. This is usually done while rendering point-clouds in geographical applications. It is a very important thing to do because after a transformation, some points may be too close to the camera and gaps between them will become visible. In general, we want to have something that resembles a continuous surface as much as possible as illustrated in figure 4.11.

This last issue together with the algorithm stated before are examples of f functions and compositions of functions that are done during the warping phase and that

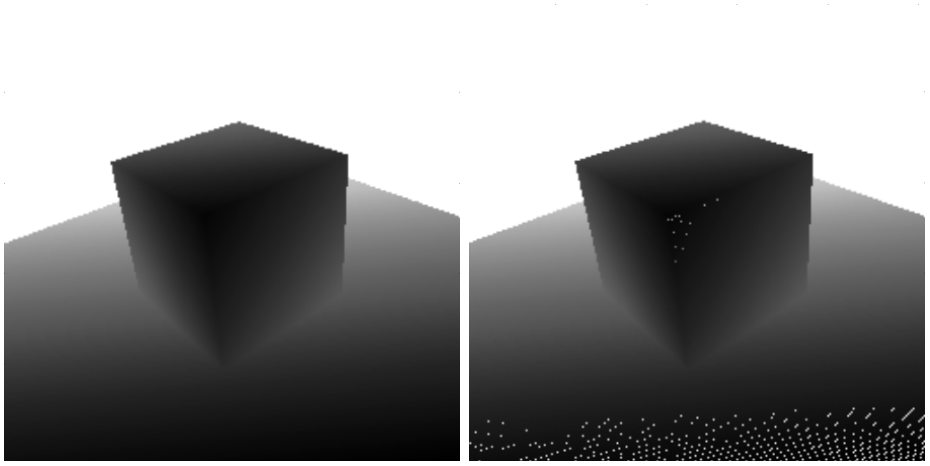

(A) No gaps when the pointcloud is denser.

(B) Gaps when the camera is close to a finer pointcloud.

FIGURE 4.11: Different pointcloud resolutions.

tend to be very difficult to differentiate analytically. This supports our idea of using numeric Jacobians for this task.

Our new version of LK and IC assume that points P are given instead of images but we also have to assume that an input image and a template image in grey-scale format, depth format or both are gathered by a camera or any other device at the beginning. These are bidimensional images that have to represent the depth or color of several sampled points so it is also required to make a prior transformation of these images into point-clouds. In order to do this a reverse.

LK and IC can be easily adapted to the new transformation and model definitions. The algorithms 3.1 and 3.2 only require the addition of an off-line step that must be done before the any other step in those algorithms. This step is the *deprojection* step which generates the associated point-cloud and their colors. In LK the deprojection must be performed over I since this is the image that is going to be warped in each iteration and it is also the image that is going to be differentiated. In IC, the deprojection is required over I and also T, I is warped at every step as well and T

is the image that is used for the Jacobian so the point-cloud is also needed. The deprojection algorithm can be executed in parallel for each pixel.

Algorithm 4.2: Deprojection algorithm in RGB-D.

Input: depth image I_d and color image I_g in grey-scale
Perspective multiply in each pixel $[i, j] \cdot \lambda$ and generate P_S
Transform P_S into P using the inverse definition of f, formally described at 4.13
Store coordinates of P and store its color value

Formal definition of the inverse projection f^{-1} or *deprojection*:

$$f^{-1} : P_S = \begin{bmatrix} j/\lambda \\ i/\lambda \\ 1/\lambda \end{bmatrix} \rightarrow P = T_{\text{6dof3D}}^{-1} \cdot C^{-1} \cdot \left[\begin{array}{c|c} K^{-1} & \bar{0} \\ \hline \bar{0} & 1 \end{array}\right] \cdot \begin{bmatrix} P_S \\ 1 \end{bmatrix} \tag{4.13}$$

Note that in these formal definitions P_S carries the depth values λ so that the actual values are calculated after doing the perspective multiply.

The deprojection could also be done online in LK. In principle, it is also possible to deproject the input image, project it again after the parameters have been updated, then deproject this new image again and so on. The problem of this approach is twofold. The computational cost becomes very high in comparison and even more importantly, each time that these points are deprojected and projected again, the errors accumulate especially for the fact that the points target a pixel and its neighbors. The latter makes objects become bigger in each step since they occupy more pixels in the image and this also accumulates. But even without this accumulation, once a projection is done, many points are rejected because of two main reasons: these points may be projected outside the screen so there is no point in rendering it or this point can be completely occluded by another point.

These are the minima (plus some details like the neighbor pixels) required to implement direct methods with RGB-D based images. However, there are other issues

that the implementer may not be aware of and they are extremely important for LK and IC to converge.

One of these issues is the coordinate system positioning since it affects the numerical conditioning of the optimization. This is a very relevant issue because of the abundance or, in contrast, lack of ambiguity that the coordinates can cause in the Jacobian. Independently of the Jacobian calculation method that is chosen, the Jacobian is theoretically meant to be an infinitely small movement that we can use to estimate qualitatively and quantitatively. In certain situations, the Jacobian of two parameters may be so similar that methods such as LK or IC cannot decide whether or not to follow one gradient, the other or both. This can happen in very simple situations, for instance, if a cube is positioned very close to the center of the coordinate system and we calculate the derivatives of a rotation over this center, the derivatives of the closest corners of the cube are going to be much higher than those from the farthest point. If the cube is far away from the center, both corners will have very similar derivatives and these derivatives can be mistaken with those from a translation (see figure 4.12, the derivatives are almost parallel when the cube is far away from the origin). Besides, if floating-points are used to simulate real numbers, the larger the number, the lesser the accuracy.

The second and last issue is related to occlusions. As stated in the examples of section 4.1, LK and IC are methods that follow the gradients (local methods) to find a local minimum or, hopefully, the global minimum. This requires that the functions that we work with are smooth enough and continuous. If LK or IC are applied to noisy images or images with sharp edges, it is unlikely that these methods will ever converge unless the rest of the image is smooth enough and these sharp points are relatively less in number than the other ones. In particular, RGB-D images are very problematic in this sense because of occlusions. Occlusions can cause images to have sharp edges that make the residuals have sharp edges, but not

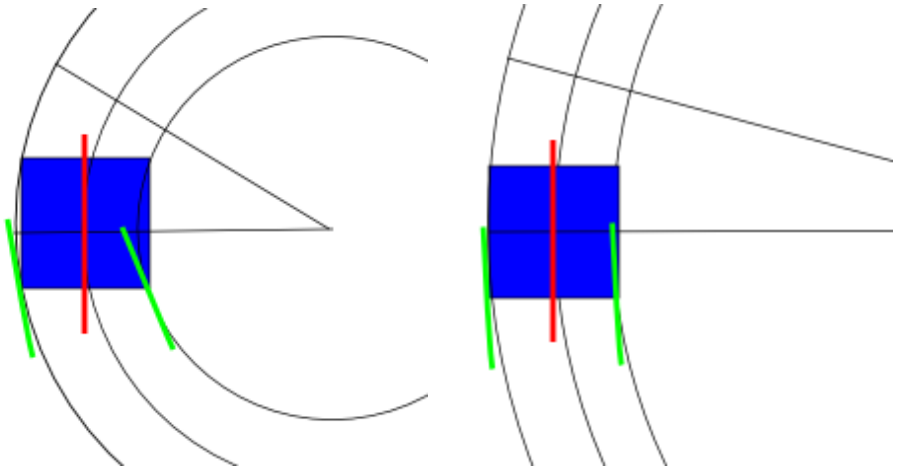

(A) Derivatives when the cube is close to the origin.

(B) Derivatives when the cube is far from the origin.

FIGURE 4.12: How different coordinate systems affect the derivatives (green for rotation derivatives and red for translation derivatives).

only that, occlusions can cause sharp edges in Jacobians as well and these are even more problematic especially in images related to depth values.

To solve this, several techniques have been proposed in the literature. These techniques are usually the robustness techniques and also coarse-to-fine schemes which can help at least when convergence acceleration is desired. These have been already presented in 3.2.4.

4.3 Synthetic models

A very brief description of the models used to perform several experiments in the RGB-D context is presented in this section. Some of these examples have only been created for experimentation purposes and are not used later in the thesis.

4.3.1 Finite plane

The finite plane may be the easiest way to test how well LK and IC perform. It can also serve to understand which ambiguities affect direct methods in RGB-D contexts.

The finite plane is a very ambiguous model when used with depth values and at the same time when it occupies the whole screen space. The depth values of an infinite plane remain the same after several sorts of warps. Definitely, warps like any rotation of the plane over its normal vector or any translation of the plane over itself or the combination of both yields another plane with the same exact depth values. Other warps do not share this problem.

When color is added to the plane, warps start being less ambiguous as long as the images used for the colors are not relatively ambiguous by themselves. For example, if an image of a circle is chosen, rotations over the center of this circle are still ambiguous even if the circle is the texture of a plane. In general, any ambiguity in a 2D scenario will still be ambiguous in a 3D plane in the same warps noted before with the depth values. Cases like this one support the idea of using depth and color data together so that ambiguities from some data are relaxed by other data.

This model has been created for the cube that is going to be employed to analyze LK and IC behavior. In case the reader is interested, the article [35] offers results of several tests using a finite plane model with 4 Gaussians distributions as their texture but with no depth values.

4.3.2 Simple cube

This model simulates three faces of a cube. Those faces that are visible from the camera perspective. In case that the tests require color data, the texture applied to

each face is the 4 Gaussian distributions image already shown in figure 4.8. Note that these three faces are rendered exactly in the same way as the finite plane but using three finite planes instead of one.

This cube is positioned in space in the following way. The cube's edges are aligned with the positive XYZ axis and the visible corner in the images is actually the coordinate origin $[0, 0, 0]$. The cube's three main and visible faces occupy all the values (depending on the sample resolution) from 0 to 1 in the XYZ positive axis.

This model has been chosen for extensive testing because a cube can be rendered having one of its faces almost perpendicularly to the camera while the other faces are in very extreme and unfavorable conditions for algorithms based on direct methods.

The camera has been zoomed and centered in one of the corners of the cube and oriented in parallel with the diagonal axis of the cube. This helps to avoid sharp edges due to silhouettes and occlusions against the background in depth images (see figures 4.13 and 4.14, note that in depth images, darker colors are closer to the camera than brighter colors). Grey scale images do not have the same problems since by default the background is set to black and the textures that are used are very dark near the edges. Furthermore, the Jacobians are calculated using the whole image while the actual image used for the residuals is a reduced version of the original image. This means that the original image is processed normally, but when the increment has to be finally calculated, a smaller window selection inside the image is used. This helps to avoid sharp edges generated after performing relatively small warps due to the lack of information outside the image.

The input image is always rendered from the "resting" position which is depicted in (A) and (B) in figure 4.13. Then the template image is generated from a vector of parameters introduced by the user. This is done in this way because if there was a case in which the cube had a face that occupied only one pixel of width, only a straight line of points would be sampled from that face. With these samples, the

point cloud is generated (see 4.2.2 for more details about the deprojection algorithm) and it would have only a straight line of samples when the underlying model is a plane. If the cube occupies always the entire rendering target (the input image), a very high and accurate amount of samples is taken from the cube and the test can succeed.

The cube is the object that has been chosen to learn how far can LK and IC be used in RGB-D and study their convergence conditions. The results are discussed in next chapter.

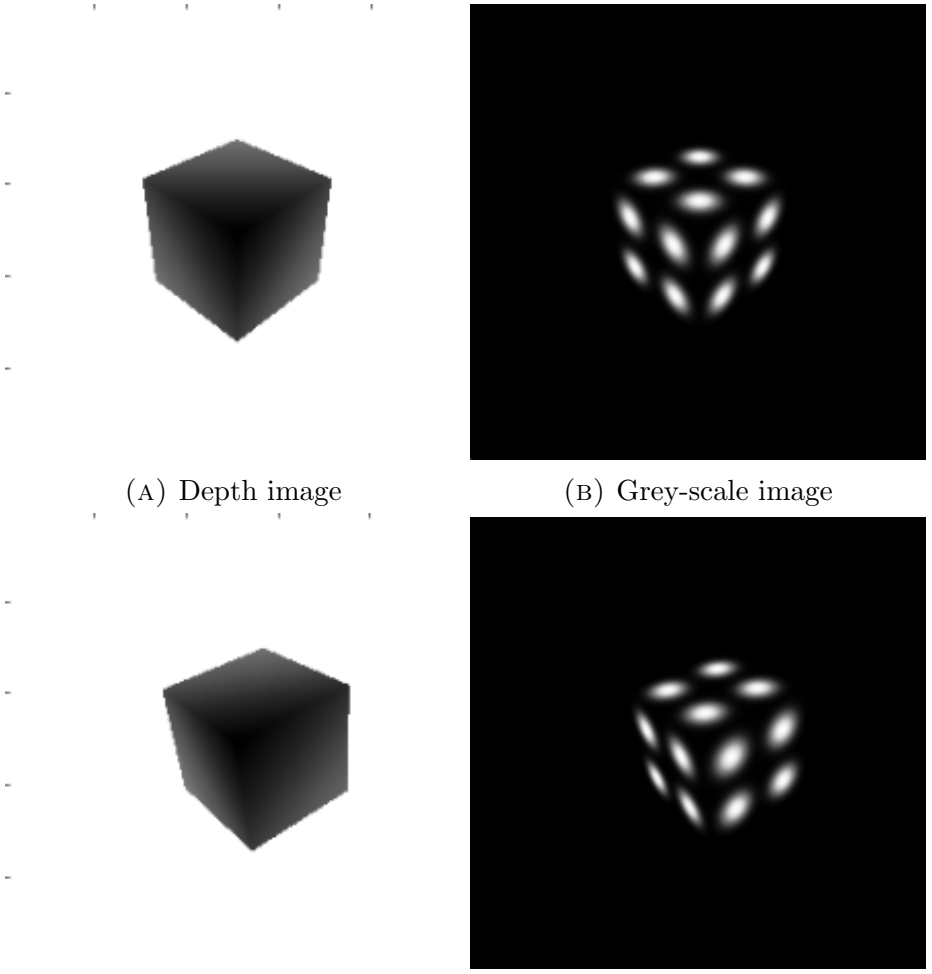

(A) Depth image (B) Grey-scale image

(C) Depth image (D) Grey-scale image

FIGURE 4.13: Examples of the cube while camera not zoomed in

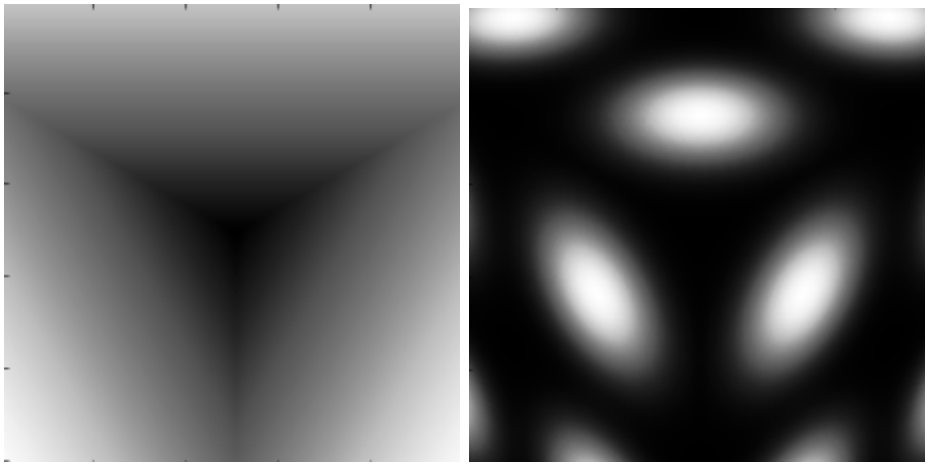

(A) Depth image (B) Grey-scale image

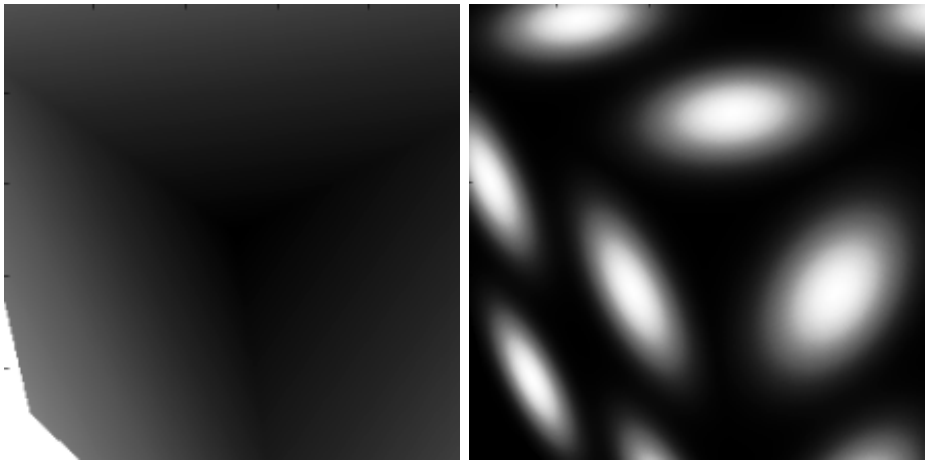

(C) Depth image (D) Grey-scale image

FIGURE 4.14: Examples of the cube while camera zoomed in

Chapter 5

Results

All the experiments have been executed using the simple cube model that has been already introduced in the methodology section 4.3. In order to understand how accurate each algorithm is in each situation, several combinations of parameters have been tested and its results have been gathered. The procedure is explained in next section.

All the tests have been executed in Ubuntu 14.04 LTS using an Intel i7-4500U CPU at 2.00 GHz. The code is written in Python 2.7.8 using NumPy 1.8.2 for fast array access together with Cython 0.20.1 for certain optimisations especially in projection and deprojection. The time has been retrieved using the *time* package available in Python's standard library. Most of the graphs and images have been generated using Matplotlib, others have been generated using Weka's visualization tab and other graphs have been generated using LibreOffice Calc.

5.1 Testing procedure

The tests have been performed using randomly sampled values for the parameters of the generated template image in different ranges. Each input and template images are generated as detailed in section 4.3 of the previous chapter. And since the inpu image is common to all the tests, that image is generated only once to accelerate the procedure.

The parameter generation procedure is similar to the one used in [35]. A total of 100 parameters are generated using random samples from a Gaussian distribution with parameters $\mu = 0$ and a desired σ ($\mathcal{N}(0, \sigma)$ offered in Python using *random.gauss* from the *random* package). For a 6 dergees of freedom transformation like those that are used in these experiments, a total of 6 parameters are required to generate the transformation. So in each test, 6 samples are gathered from that distribution and those samples are given to the testing tool to proceed. In order to be able to classify tests by difficulty, the value of σ is changed every 100 tests[1]. The values of σ are changed using the values from the set $0.01, 0.05, 0.1, 0.15, 0.2$. Since we have 2 algorithms with 3 image variants, this means that a total of 3000 tests are generated in the process.

All these tests have been executed using a derivative precision value of $h = 0.005$ and the values used as thresholds for the halting criterion in the increment are $c = 0.005$ for convergence and $d = 0.5$ for divergence. When the increment's norm has reached c or d or 20 iterations have been performed, the algorithm decides to halt. If c is reached, a convergence state is returned, when d is reached a divergence state is returned and when the 20 iterations have been reached, we cannot decide what could have happened. Additionally, if a Jacobian has a lower range, a singular matrix error is detected and the state of singular matrix is returned.

[1] Note that increasing the value of σ just makes it more likely to get larger samples, but smaller samples are still possible, this is a desired effect so that not all the parameters are equally large.

These values have been acquired after extensive testing. Though, more testing would be needed to obtain the best value for each parameter but that also depends on the case. So we have chosen the values that make the results be better in general. For instance, certain values do not even produce acceptable Jacobians or in other cases, threshold convergence values that are too large halt the algorithms too early and if a test would diverge, an early halt may make this test look like if it performed well. The maximum amount of iterations to halt the algorithm is 20. When this amount of iterations is reached, it cannot be decided if the algorithm will actually converge to a minimum (even if this is a local minimum) or not.

The first set of tests did not yield consistent results due to the fact that h was not small enough so the accuracy of the Jacobian was not leading the algorithms well when the accuracy was very close. Several graphs showed that there was noise at the end of the series of iterations.

The second set of tests had a very small h leading to singular matrices (the cluster with around 1.5 increment norm) because there were no differences between the transformations with such a low value.

After the process has finished performing the tests, some statistics are gathered so that conclusions can be drawn and explained in this chapter. The statistics that are important for us are those that measure the accuracy of our tests. The evaluation is done calculating the Euclidean distance between 3 known points ($[0, 0, 0]$, $[1, 0, 0]$ and $[0, 1, 0]$) and their 3 counterparts after being transformed by the initial transformation done in the template and then transforming these points back to their originals using our parameter estimation in the current test. The closer these points are in space, the lesser the distance will be. The distances of each pair are added to generate the measure. If the distance is too high, we say that the algorithm has not *succesfully converged* to a relatively desirable solution. This desirable solution is the *convergence threshold*.

The convergence threshold has been decided experimentally after observing the results obtained from several tests prior to the tests with different values of σ. To observe the results, two tools have been used, one is Weka's visualization tool and the other is the result visualization available in our implementation. Weka tools can be used to see where are the clusters of converging tests in general and these convergence thresholds can be deduced from them after several test results have been gathered. This set of tests have been used to guess the values of h, c and d as well. The value that is going to be used to discard tests as not successfully convergent are those surpassing a threshold of 0.2 for the 3D distance measures. Which means that at most each point has deviated $0.2/2 = 0.1$ since we are adding the distances of the three points together and at most one point will remain static while the others rotate.

To illustrate how much is 0.2 for a 3D error distance is, see figure 5.1 showing an error distance of 0.22215.

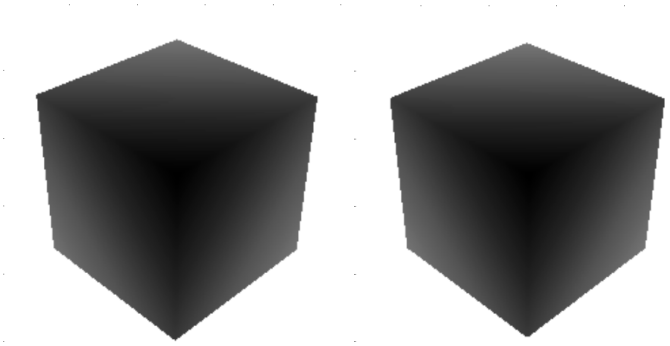

(A) Target warp (B) Estimated warp

FIGURE 5.1: Example of a warp discarded because of its error.

5.2 Results analysis

This section provides the results and summaries obtained from the various tests already described in the testing procedure.

5.2.1 Test sets

The cluster images that were analyzed to finally opt to certain parameters provided a good idea of how all the algorithms perform in general terms and what the tendency is. The first set of tests with relatively close parameters provided a very good feedback because of the graph clarity, see figure 5.2. It can be noted that most of the succesful results are gathered within a very tight cluster where most cases halted with relatively low increments. The figure shows the whole dataset in two axis where the horizontal axis is the 2D error distance and the vertical axis is the 3D distance error that each instance ended with. Each color shows the type of algorithm and image that was used in that test (dark-blue for LK_d, red for LK_g, green for LK_{gd}, light-blue for IC_d, light pink for IC_g and dark pink for IC_{gd} where "d" refers to only depth images, "g" refers to only grey images and "gd" means both).

The amount of failed tests for LK was unexpected especially in the depth images only. To understand why these tests failed, a couple of examples and detailed comparisons of the results are shown.

A first example is LK depth with parameters $[0.3, 0.3, 0, 0, 0, 0]$. It is compared with the test that has parameters $[0.2, 0.2, 0, 0, 0, 0]$ which is sufficient for our purposes. This is shown in figures 5.3 and 5.4. In the first image, the centered window does not have any pixel with values of the background. On the other hand, the second image has a large portion of background pixels.

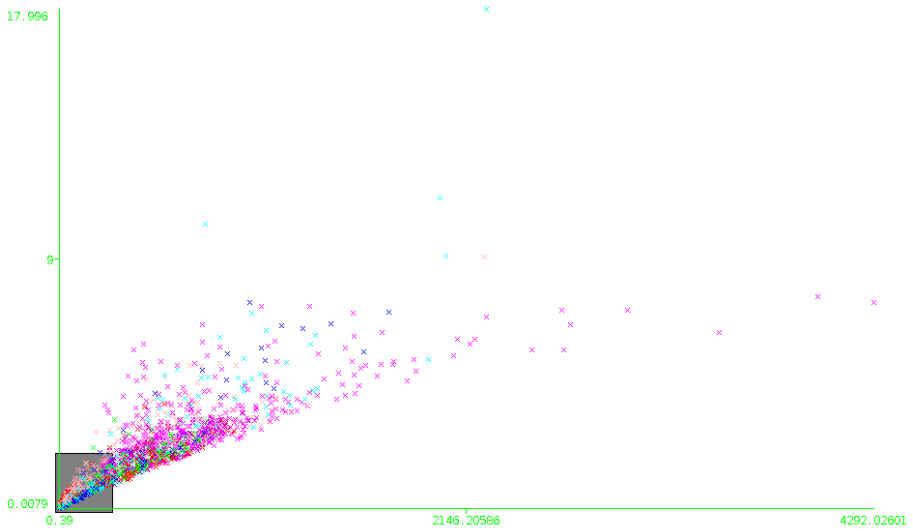

(A) Whole dataset

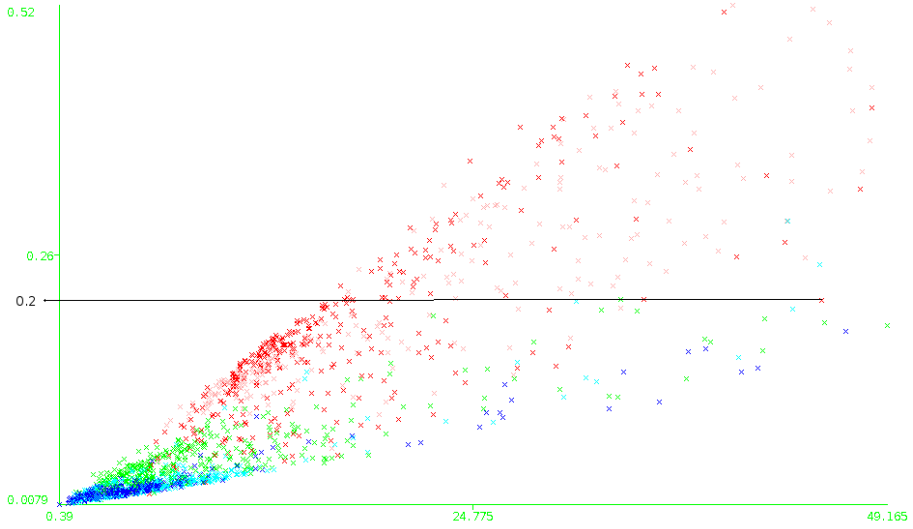

(B) Subset that converges

FIGURE 5.2: Graphs showing the relationship between 2D and 3D error distances.

In the first iteration of LK in the case of $[0.3, 0.3, 0, 0, 0, 0]$, one realises that the Jacobians are not suitable for good convergence because of the large discrepancy between the residual and the Jacobians. This discrepancy has a visible effect in the

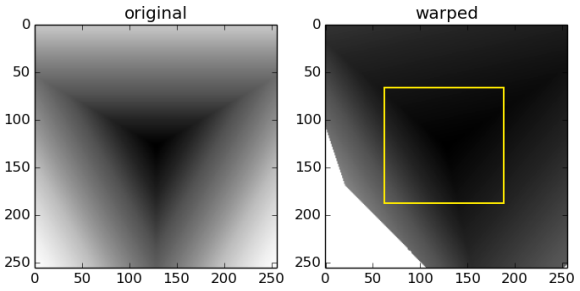

(A) Original image used as input image and its warped image as template.

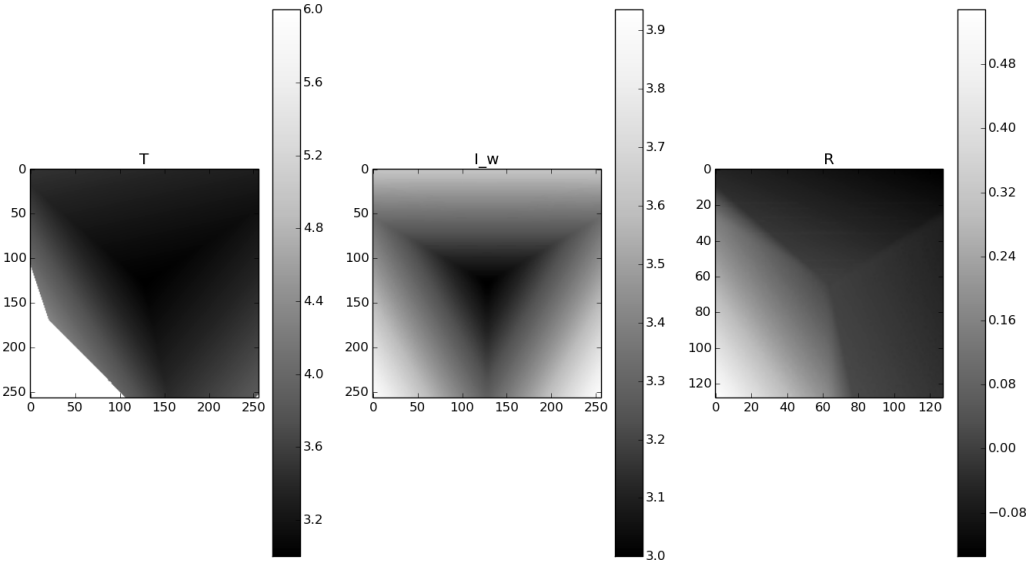

(B) Residual of previous image (inside the window).

FIGURE 5.3: Warp of $[0.2, 0.2, 0, 0, 0, 0]$, original images and their residuals.

proportional product (the distintion between the two products is given in section 4.1). Figure 5.5 illustrates this, the forth parameter's derivatives is the one named "Jp4". The parameter "p4" is the responsible of the translations in the X axis of the object (from left to right in the images).

When the per-pixel product (theoretically, per point) is done between the derivatives and the residuals, the image called "prop4" is generated. This image is the first product that was distinguished in two very simple cases in section 4.1. This image

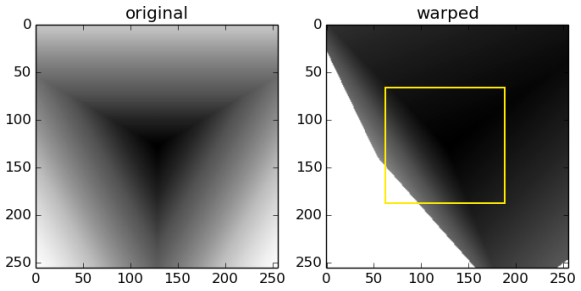

(A) Original image used as input image and its warped image as template.

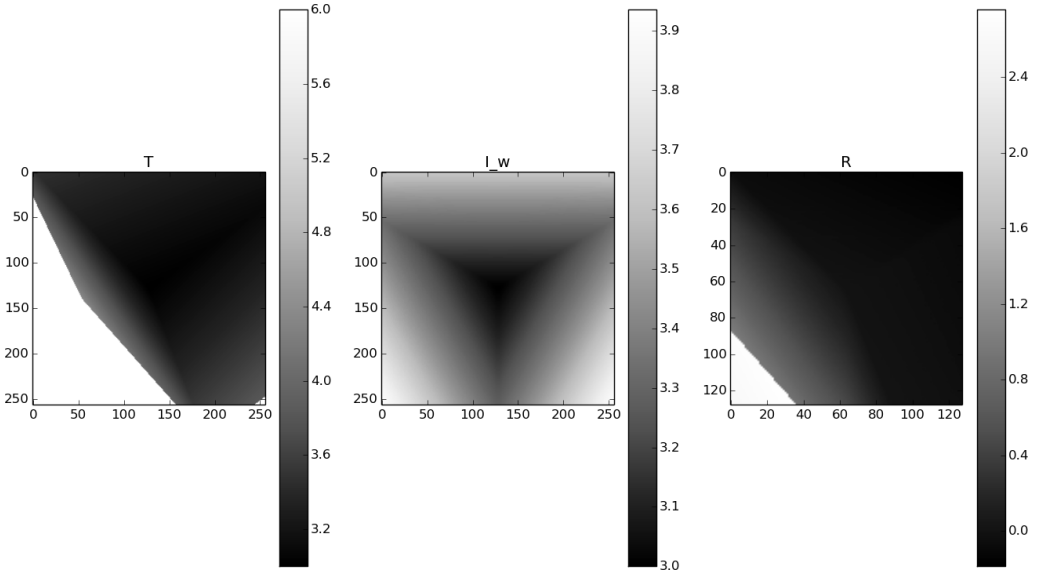

(B) Residual of previous image (inside the window).

FIGURE 5.4: Same graph showing this time a warped image made using $[0.3, 0.3, 0, 0, 0, 0]$ as the template.

is directly proportional to the final outcome of $\delta\mu$. The inverse part is shown as the Hessian matrix of all the parameters which has already been inverted in those images, so the one shown there is already proportional to $\delta\mu$ instead.

The image "prop4" is very smooth in general except in the area related to the background. This area has very small negative values while the rest of the image has mostly negative to nearly neutral values. If this is compared to the same one in

$[0.2, 0.2, 0, 0, 0, 0]$, the difference is tangible. Obviously, both examples have exactly the same Hessian matrix in LK and the vectors of the proportional part of each parameter are also very similar apparently in those images. If one looks closer, the values in provided in the right side color bars for each plot, the values are much more distant than those from the easier example shown in figure A. These values are relatively more negative and their absolute value is much larger than the others. Since the Hessian is the same, it is clear at this point that the increment $\delta\mu$ of the example with background is going to be much more exaggerated due to the simple fact that the background was present.

These effects of the background in the IC are less noticeable. Figure 5.6 shows the information as the figures that were referenced before but in IC with parameters $[0.3, 0.3, 0, 0, 0, 0]$. It is still the first iteration in the algorithm. It can be noted that the values are very extreme starting with the Jacobian. There is no relative smoothness and there only exists a single sharp edge, the one between the cube and the background. The Jacobian in IC is very different this time because the information is provided by the target instead of the starting point. All the values are extreme in all the Jacobian images for every parameter, that is the reason behind such small values in the Hessian matrix. The difference in orders of magnitude between the Hessian values and the porportional vector values is much more pronounced than the difference in LK, even in the difference in LK for the easier example. This entails that the convergence or divergence of this example is very slow. Since a maximum of 20 iterations is set, the algorithm does not diverge as fast as LK does. It is our belief that this is the main explanation behind those divergent cases in LK shown in figure 5.2. Besides, this does not happen in grey-scale images because the background is black and the textures are mostly black in the edges.

The results of these examples in $[0.3, 0.3, 0, 0, 0, 0]$ with LK and IC are presented in figure 5.7.

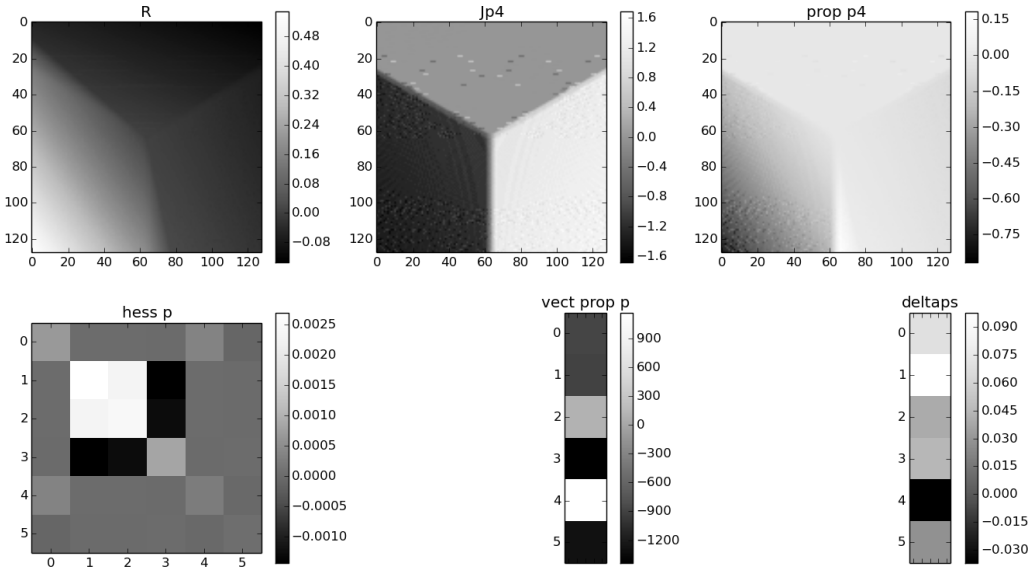

(A) Jacobian in LK with warp $[0.2, 0.2, 0, 0, 0, 0]$.

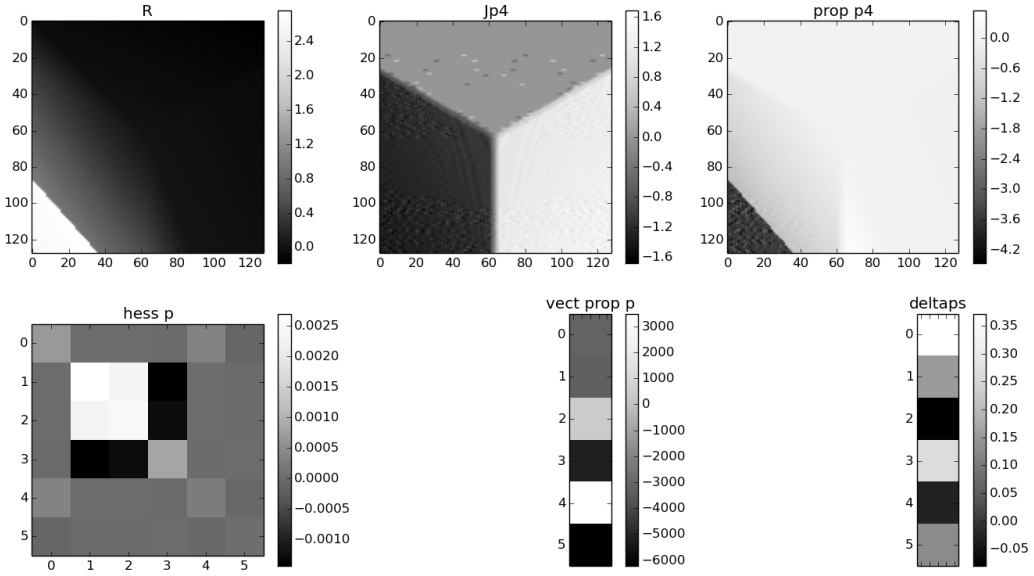

(B) Jacobian in LK with warp $[0.3, 0.3, 0, 0, 0, 0]$.

FIGURE 5.5: Comparison of Jacobians in both examples.

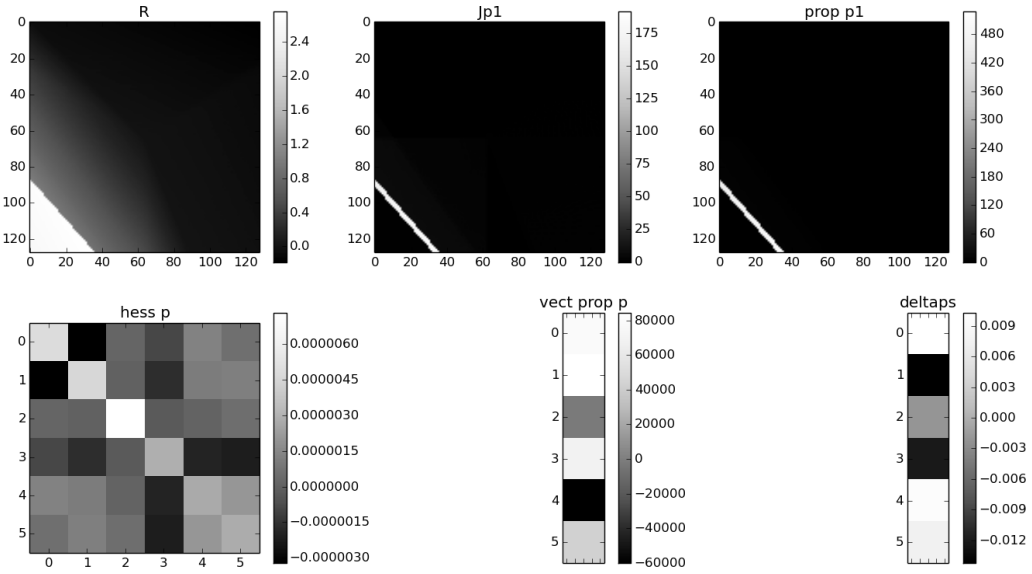

FIGURE 5.6: Again the same graph but in IC.

5.2.2 Overall results

These are the overall results obtained from the 3000 tests set that has been explained in detail before. The overall results are shown following the same ideas of three plots proposed in [35]. Each plot describes:

- **Robustness plot**: this plot shows the percentage of successes that have been found in our tests for each algorithm and type of image and σ (figure 5.8).
- **Accuracy plot**: for those tests that have successfully converged, the accuracy is compared also with varying σ (figure 5.9).
- **Rate of convergence plot**: in this plot, also the successful tests are taken into account. The plot shows regardless of the value of σ the accuracy (error distance) of each algorithm in each kind of image (figure 5.10).

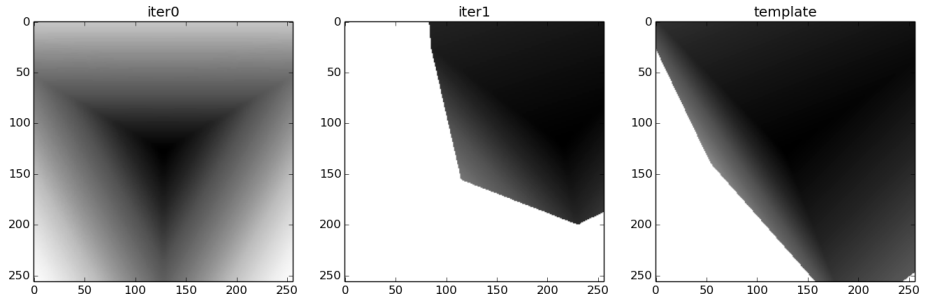

(A) Input, resulting and template images in LK example.

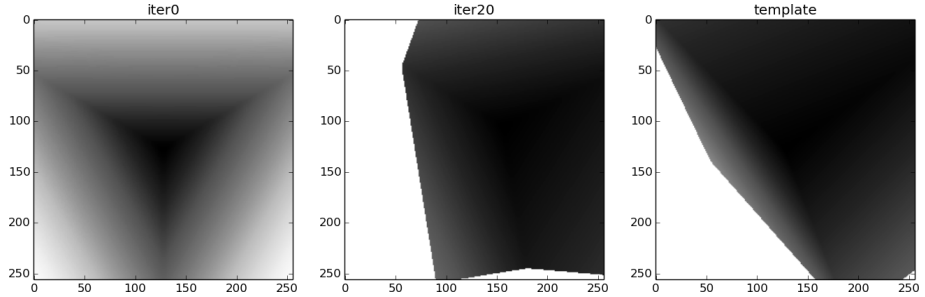

(B) Input, resulting and template images in IC example.

FIGURE 5.7: Comparison of images in the example with parameters $[0.3, 0.3, 0, 0, 0, 0]$.

The robustness plot shows clearly that all the algorithms that use depth values tend to work better than those based on grey-scale images. This confirms that depth values are indeed good sources of information to estimate transformations of rigid bodies. The reader should note that the warps at higher values of σ tend to be very complicated to estimate so it is just logical that the results of all algorithms tend to decrease in a very constant pace. As expected Lucas-Kanade offers the best results in every combination against those from IC. Though IC is very close to LK when used together with depth images. So this also confirms that IC can be used for image alignment tasks using depth images.

Unfortunately, it seems that IC cannot work well in any case when mixing both sorts of images. This was actually an unexpected result so a question remains open, we still do not know how to combine well both data so that it works better in IC.

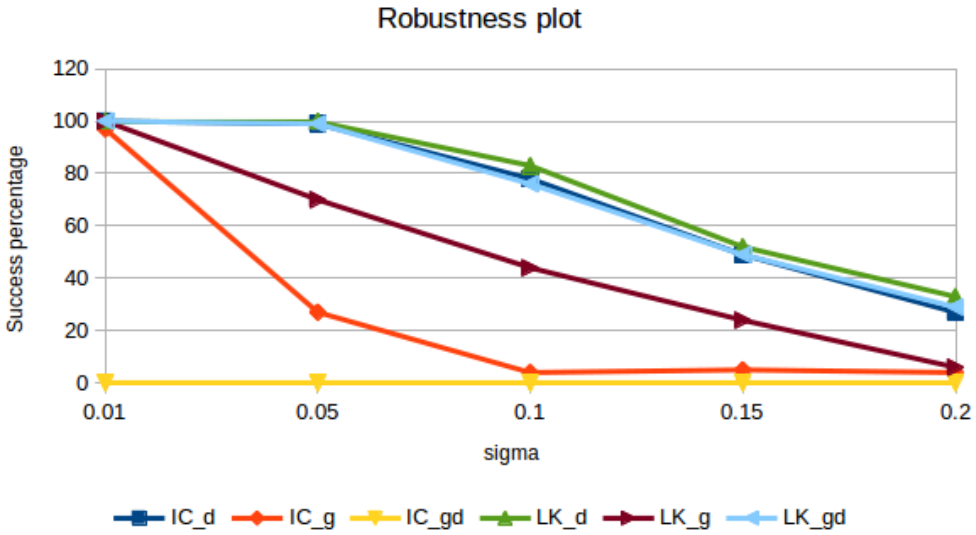

FIGURE 5.8: Robustness plot

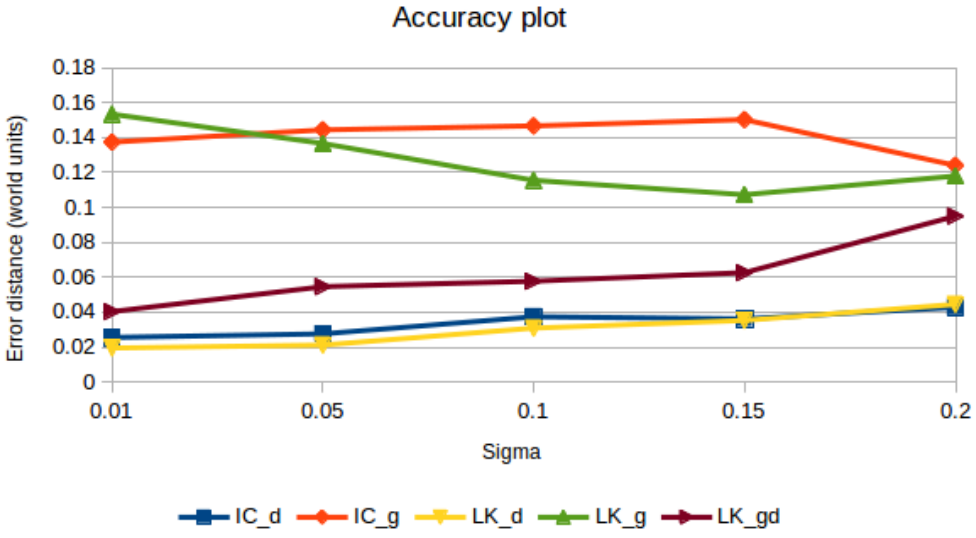

FIGURE 5.9: Accuracy plot

IC performs very well with depth images so the expected behavior would be that depth images would compensate for the bad results obtained in IC with grey-scale

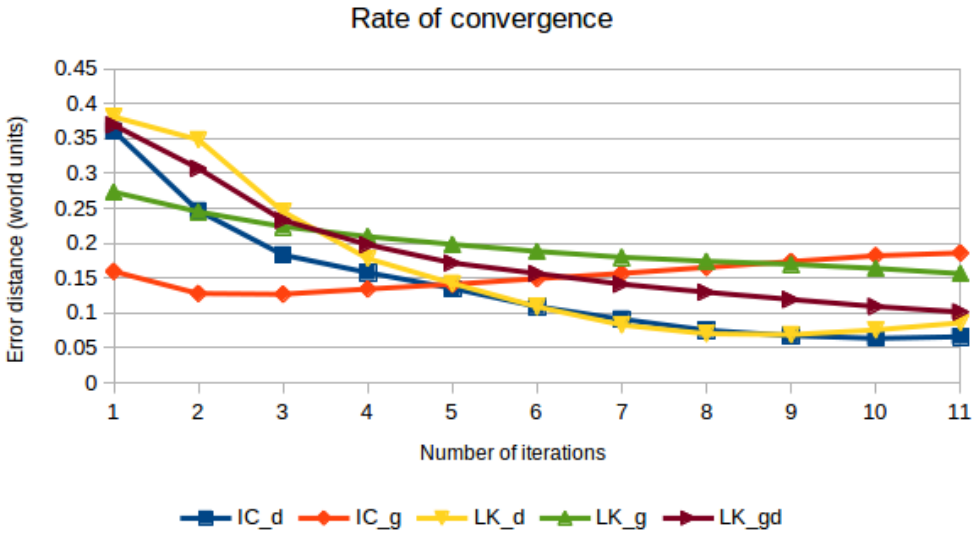

FIGURE 5.10: Rate of convergence plot

values. The reason behind this is likely to be the fact that IC cannot work well with grey scale images as stated in [35] because it does not satisfy the EBCA condition. It seems that the grey values can be very confusing and any sort of alteration can lead to very unstable results such as this one.

LK appears to perform poorly especially in comparison to the results obtained with depth images. In this case, LK does actually benefit from depth data since it performs as well as those with just depth data. So it is very clear at this point that grey-scale values are not a very good option to estimate 3D transformations as a whole. Not even images that are as smooth as the ones used in these tests. This may seem to contradict our thoughts about LK. LK was supposed to perform well in every scenario, even though it was expected that the worst scenario would be the grey scale images. But there is a plausible explanation behind this. If the accuracy plot is checked, IC with grey values seems to be getting a worse accuracy with every sigma increase while curiously, the opposite happens with LK. The last sigma (0.2) does not count as much in this plot for LK_g, IC_g or LK_{gd} because this average was

calculated from just 4 to 6 tests that passed the convergence criterion[2]. Note that in the robustness plot and in the rate of convergence plot IC_{gd} does not even exist in these plots because there are no tests that have succesfully converged.

Finally, the last plot, the rate convergence, shows a very clear result that summarizes and cofirms all the assumptions. It seemed confusing that IC_g could have so good results and especially so close to LK_g. However, this is just apparent. When figure 5.10 is analyzed, it is clear that all the tests that have been classified as succesful start on average with a more difficult situation (the error at the beginning is higher) than LK_g but especially than IC_g. IC_g tests that succesfully converge start with a distance that is even smaller than the criterion on average so the algorithm just needs to converge close to the starting point and the results will of course be very satisfactory. But even with such an advantage, these tests that converge actually tend to diverge over time since the graph shows that the error tends to increase while in the other algorithms decrease. This graph also shows that LK_g converges but maybe 20 iterations before halting is not enough for LK_g to converge well. So in any case, this graph shows that using grey-scale images for these tasks is counterproductive in general.

[2]Check the robustness plot to see that all these tests are close to a 0 percent and therefore, if a couple of tests have relatively large values or relatively small, the average is seriously affected

Chapter 6

Conclusions

In general the experiments have confirmed our first impression that depth images serve as a good guidance for direct methods towards a global optimum, mainly because of their smoothness. The difference between the accuracy obtained from depth values and the accuracy obtained from grey scale values is even more significative because of the lack of difficulty in the synthetic tests that have been proposed and used. This was expected and now is confirmed.

There is one detail that was not entirely expected. The experiments have also shown that combining both images equally (using the *extended image* definition from [26]) does not work as well as we thought it would at the beginning of the research process. It was expected that when combining both images, the depth data would have a better effect over the algorithm's outcome in comparison to grey scale data on its own. But the results show that in IC this is not the case and the results are the worst by far.

The results have also confirmed our most relevant hypothesis, that IC performs very well in depth images but that it is not suitable for grey scale images. This was already known from the studies done in [35] according to the theory behind

the EBCA. LK outperforms IC in all the tests where grey scale data is involved. As it has already been stated, IC is seriously affected by grey scale values and the increment step seems to get contaminated to the point that it tends to slowly diverge. In our data, the convergence of IC with grey scale images is reasonable but that is because of the fact that there is a maximum amount of iterations and the process has not been tested long enough to actually make the algorithm to lie outside the convergence threshold that we have established. However, according to our results, the convergence of IC in these images decreases substantially as the iterations advance but the other methods do not share this problem.

These results will let future students or researchers study and address the particular problems that have been detected for each algorithm and each case to mitigate these problems using other techniques in conjunction with these algorithms.

6.1 Future work

Several lines of future work are opened for further research. Each one of the ideas that were out of the scope of this thesis are detailed in the following list:

- It is necessary to perform more tests but using different models and especially different textures for the grey-scale images. These models should be more challenging than a cube so that further studies can be made in order to understand better the behavior of these algorithms.
- Since the high contrast between the depth of the background and the depth of the object lead to mistakes, it is necessary to at least create an algorithm that solves this issue and afterwards, these tests could be reused to see if the algorithm is capable of improving the results in comparison to the results obtained here.

- These tests could be accelerated so that the implementation could be used even in real-time with data retrieved from a depth camera.

Appendix A

Kinect and OpenCV

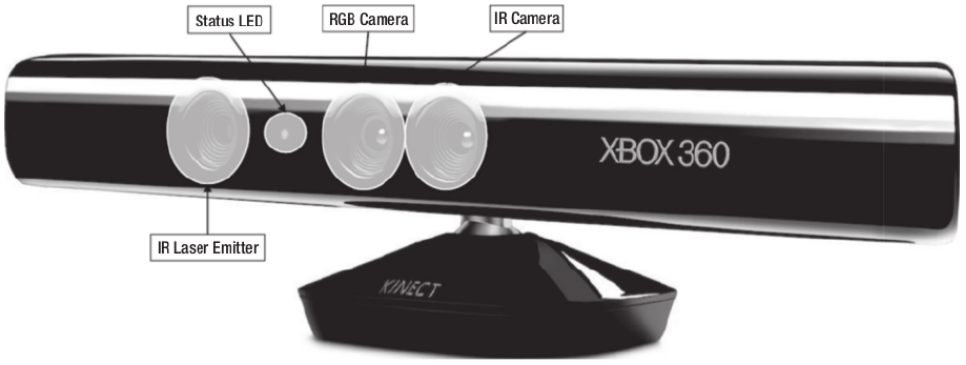

FIGURE A.1: The Kinect device.

The installation of the Kinect device for Ubuntu OS is detailed in this appendix. The installation procedure has been tested in April 2015 in a system with Ubuntu 14.04 LTS installed. This procedure should be also very similar for other Linux distributions.

In order to install and use the Kinect device, at least one USB connection is required. The software needed prior to the main installation process can be installed using the following command (these are not multiple commands but a large single command).

```
sudo apt-get install git-core cmake freeglut3-dev \\
pkg-config build-essential libxmu-dev libxi-dev \\
libusb-1.0-0-dev doxygen graphviz mono-complete
```

The following procedure is the one needed to install the device via OpenNI and OpenCV:

Installation of OpenNI 1.5.x, type the following commands in a terminal from your home directory or any other place where the OpenNI's source repository is going to be downloaded:

```
mkdir ~/kinect
cd ~/kinect
git clone https://github.com/OpenNI/OpenNI.git
cd OpenNI/Platform/Linux/CreateRedist/
chmod +x RedistMaker
./RedistMaker
cd ../Redist/OpenNI-Bin-Dev-Linux-x64-v1.5.7.10/
sudo ./install.sh
```

Download PrimeSense drivers for Kinect from a repository as well:

```
cd ~/kinect/
git clone git://github.com/avin2/SensorKinect.git
```

Before installing, change 2 files using the code available at https://github.com/avin2/SensorKinect/pull/5/files#diff-181b87ab5e036090aa9a6cb65e715212 (checked site availability in July 2015). Then substitute the files under source/XnDeviceSensorV2 with those available at the given URL.

Proceed with the installation of the drivers:

```
cd SensorKinect/Platform/Linux/CreateRedist/
chmod +x RedistMaker
./RedistMaker
cd ../Redist/Sensor-Bin-Linux-x64-v5.1.0.25/
chmod +x install.sh
sudo ./install.sh
```

Installation of OpenCV using the latest stable version available at http://sourceforge.net/projects/opencvlibrary/ (checked site availability in July 2015). Then uncompress it and do the following in the directory:

```
cd ~/opencv-2.4.11/
mkdir release
cd ./release/
cmake -D WITH_OPENNI=ON ..
```

Check that OpenNI and PrimeSense modules have the flag "yes" in the ending summary, then:

```
make
sudo make install
```

Finally, install the non-free OpenCV modules:

```
sudo add-apt-repository --yes ppa:xqms/opencv-nonfree
sudo apt-get update
sudo apt-get install libopencv-nonfree-dev
```

After this, the Kinect sensor should be available as an accessible class via C++ named *VideoCapture* in OpenCV. Some code samples to access to the data are provided at http://docs.opencv.org/doc/user_guide/ug_highgui.html. This class allows the user not only to collect image data from the sensor but also to access some of the device's internal information such as calibration data or to enable lense distortion correction.

Alternatively, it is also possible to calibrate the Kinect sensor to get your own version of the intrinsic parameters of the cameras. In order to do so, there is practical guide that explains in detail the steps that have to be followed, see reference [40].

There are other ways to access, for example, OpenKinect is another library that can access the Kinect data streams but not the calibration data nor other internal information of the device. The installation process is much simpler and it can also be found at [40]. OpenKinect provides wrappers to several languages and it is very easy to use. There are interesting examples available at https://github.com/amiller/libfreenect-goodies (checked site availability in July 2015).

Another alternative is to use the ROS (Robotics Operating System) packages at http://wiki.ros.org/Packages (checked site availability in July 2015). The Kinect interface to access within ROS and the drivers are available at http://wiki.ros.org/freenect_stack. They also have detailed instructions about how to calibrate RGB cameras and, in particular, the depth sensor http://wiki.ros.org/kinect_node/Calibration (checked site availability in July 2015).

Bibliography

[1] Enrique Muñoz Corral. *Efficient Model-based 3D Tracking by Using Direct Image Registration*. PhD thesis, Facultad de Informatica, 2012.

[2] Richard Szeliski and Heung-Yeung Shum. Creating full view panoramic image mosaics and environment maps. In *Proceedings of the 24th annual conference on Computer graphics and interactive techniques*, pages 251–258. ACM Press/Addison-Wesley Publishing Co., 1997.

[3] Richard Szeliski. Image alignment and stitching: A tutorial. *Foundations and Trends® in Computer Graphics and Vision*, 2(1):1–104, 2006.

[4] Carol Martinez, Luis Mejias, and Pascual Campoy. A multi-resolution image alignment technique based on direct methods for pose estimation of aerial vehicles. In *Digital Image Computing Techniques and Applications (DICTA), 2011 International Conference on*, pages 542–548. IEEE, 2011.

[5] George Papandreou and Petros Maragos. Adaptive and constrained algorithms for inverse compositional active appearance model fitting. In *Computer Vision and Pattern Recognition, 2008. CVPR 2008. IEEE Conference on*, pages 1–8. IEEE, 2008.

[6] Lisa Gottesfeld Brown. A survey of image registration techniques. *ACM computing surveys (CSUR)*, 24(4):325–376, 1992.

[7] Barbara Zitova and Jan Flusser. Image registration methods: a survey. *Image and vision computing*, 21(11):977–1000, 2003.

[8] JB Antoine Maintz and Max A Viergever. A survey of medical image registration. *Medical image analysis*, 2(1):1–36, 1998.

[9] Bruce D Lucas, Takeo Kanade, et al. An iterative image registration technique with an application to stereo vision. In *IJCAI*, volume 81, pages 674–679, 1981.

[10] Gregory D Hager and Peter N Belhumeur. Efficient region tracking with parametric models of geometry and illumination. *Pattern Analysis and Machine Intelligence, IEEE Transactions on*, 20(10):1025–1039, 1998.

[11] Heung-Yeung Shum and Richard Szeliski. Systems and experiment paper: Construction of panoramic image mosaics with global and local alignment. *International Journal of Computer Vision*, 36(2):101–130, 2000.

[12] Simon Baker and Iain Matthews. Equivalence and efficiency of image alignment algorithms. In *Computer Vision and Pattern Recognition, 2001. CVPR 2001. Proceedings of the 2001 IEEE Computer Society Conference on*, volume 1, pages I–1090. IEEE, 2001.

[13] He Zhao. Inverse compositional method.

[14] Simon Baker and Iain Matthews. Lucas-kanade 20 years on: A unifying framework. *International journal of computer vision*, 56(3):221–255, 2004.

[15] Freédeéric Jurie and Michel Dhome. Hyperplane approximation for template matching. *Pattern Analysis and Machine Intelligence, IEEE Transactions on*, 24(7):996–1000, 2002.

[16] Alper Yilmaz, Omar Javed, and Mubarak Shah. Object tracking: A survey. *Acm computing surveys (CSUR)*, 38(4):13, 2006.

[17] Yi Wu, Jongwoo Lim, and Ming-Hsuan Yang. Online object tracking: A benchmark. In *Computer vision and pattern recognition (CVPR), 2013 IEEE Conference on*, pages 2411–2418. IEEE, 2013.

[18] Zheng Fang and Yu Zhang. Experimental evaluation of rgb-d visual odometry methods. *International Journal of Advanced Robotic Systems*, 12, 2015.

[19] Richard A Newcombe, Shahram Izadi, Otmar Hilliges, David Molyneaux, David Kim, Andrew J Davison, Pushmeet Kohi, Jamie Shotton, Steve Hodges, and Andrew Fitzgibbon. Kinectfusion: Real-time dense surface mapping and tracking. In *Mixed and augmented reality (ISMAR), 2011 10th IEEE international symposium on*, pages 127–136. IEEE, 2011.

[20] Shahram Izadi, David Kim, Otmar Hilliges, David Molyneaux, Richard Newcombe, Pushmeet Kohli, Jamie Shotton, Steve Hodges, Dustin Freeman, Andrew Davison, et al. Kinectfusion: real-time 3d reconstruction and interaction using a moving depth camera. In *Proceedings of the 24th annual ACM symposium on User interface software and technology*, pages 559–568. ACM, 2011.

[21] Carl Yuheng Ren and Ian Reid. A unified energy minimization framework for model fitting in depth. In *Computer Vision–ECCV 2012. Workshops and Demonstrations*, pages 72–82. Springer, 2012.

[22] Carl Yuheng Ren, Victor Prisacariu, Derek Murray, and Ian Reid. Star3d: simultaneous tracking and reconstruction of 3d objects using rgb-d data. In *Computer Vision (ICCV), 2013 IEEE International Conference on*, pages 1561–1568. IEEE, 2013.

[23] Maxime Meilland, Andrew Comport, Patrick Rives, et al. A spherical robot-centered representation for urban navigation. In *Intelligent Robots and Systems (IROS), 2010 IEEE/RSJ International Conference on*, pages 5196–5201. IEEE, 2010.

[24] Maxime Meilland, Andrew Ian Comport, and Patrick Rives. Dense visual mapping of large scale environments for real-time localisation. In *Intelligent Robots and Systems (IROS), 2011 IEEE/RSJ International Conference on*, pages 4242–4248. IEEE, 2011.

[25] Tommi Tykkälä, Cédric Audras, Andrew Comport, et al. Direct iterative closest point for real-time visual odometry. In *Computer Vision Workshops (ICCV Workshops), 2011 IEEE International Conference on*, pages 2050–2056. IEEE, 2011.

[26] Cedric Audras, A Comport, Maxime Meilland, and Patrick Rives. Real-time dense appearance-based slam for rgb-d sensors. In *Australasian Conf. on Robotics and Automation*, 2011.

[27] Christian Kerl, Jurgen Sturm, and Daniel Cremers. Robust odometry estimation for rgb-d cameras. In *Robotics and Automation (ICRA), 2013 IEEE International Conference on*, pages 3748–3754. IEEE, 2013.

[28] Christian Kerl, Jurgen Sturm, and Daniel Cremers. Dense visual slam for rgb-d cameras. In *Intelligent Robots and Systems (IROS), 2013 IEEE/RSJ International Conference on*, pages 2100–2106. IEEE, 2013.

[29] Jürgen Sturm, Nikolas Engelhard, Felix Endres, Wolfram Burgard, and Daniel Cremers. A benchmark for the evaluation of rgb-d slam systems. In *Intelligent Robots and Systems (IROS), 2012 IEEE/RSJ International Conference on*, pages 573–580. IEEE, 2012.

[30] Kevin Lai, Liefeng Bo, Xiaofeng Ren, and Dieter Fox. A large-scale hierarchical multi-view rgb-d object dataset. In *Robotics and Automation (ICRA), 2011 IEEE International Conference on*, pages 1817–1824. IEEE, 2011.

[31] Youngmin Park, Vincent Lepetit, and Woontack Woo. Texture-less object tracking with online training using an rgb-d camera. In *Mixed and Augmented*

Reality (ISMAR), 2011 10th IEEE International Symposium on, pages 121–126. IEEE, 2011.

[32] Michael Krainin, Peter Henry, Xiaofeng Ren, and Dieter Fox. Manipulator and object tracking for in-hand 3d object modeling. *The International Journal of Robotics Research*, 30(11):1311–1327, 2011.

[33] Jörg Stückler and Sven Behnke. Model learning and real-time tracking using multi-resolution surfel maps. In *AAAI*, 2012.

[34] Richard Hartley and Andrew Zisserman. *Multiple view geometry in computer vision*. Cambridge university press, 2003.

[35] Enrique Muñoz, Pablo Márquez-Neila, and Luis Baumela. Rationalizing efficient compositional image alignment. *International Journal of Computer Vision*, 112(3):354–372, 2015.

[36] Jean-Yves Bouguet. Pyramidal implementation of the affine lucas kanade feature tracker description of the algorithm. *Intel Corporation*, 5:1–10, 2001.

[37] Frank Steinbrücker, Jürgen Sturm, and Daniel Cremers. Real-time visual odometry from dense rgb-d images. In *Computer Vision Workshops (ICCV Workshops), 2011 IEEE International Conference on*, pages 719–722. IEEE, 2011.

[38] Sebastian Klose, Peter Heise, and Aaron Knoll. Efficient compositional approaches for real-time robust direct visual odometry from rgb-d data. In *Intelligent Robots and Systems (IROS), 2013 IEEE/RSJ International Conference on*, pages 1100–1106. IEEE, 2013.

[39] David Jiménez-Cabello. *Correction of Errors in Time of Flight Cameras*. PhD thesis, Universidad de Alcalá, Escuela Politécnica Superior, Departamento de Electrónica, 2015.

[40] Marina von Steinkirch. Introduction to the microsoft kinect for computational photography and vision. 2013.